



Peer review status:

This is a non-peer-reviewed preprint submitted to EarthArXiv.

# Neoproterozoic denudation of a Laurentian superbasin

Kalin T. McDannell<sup>1,2</sup>, C. Brenhin Keller<sup>2</sup>, Robert H. Rainbird<sup>3</sup>, Keith Dewing<sup>4</sup>, Jeremy W. Powell<sup>3</sup>, Paul B. O’Sullivan<sup>5</sup>

<sup>1</sup>Department of Earth & Climate Sciences, Bates College, Lewiston ME 03440, USA

<sup>2</sup>Department of Earth Sciences, Dartmouth College, Hanover, NH 03755, USA

<sup>3</sup>Natural Resources Canada, Geological Survey of Canada, Ottawa ON K1A 0E8, Canada

<sup>4</sup>Natural Resources Canada, Geological Survey of Canada, Calgary, AB T2L 2A7, Canada

<sup>5</sup>GeoSep Services, 1521 Pine Cone Road, Moscow, ID 83843, USA

## Key Points:

- This study supports the ‘superbasin hypothesis’ of interconnected Proterozoic sedimentary basins across northern Canada
- Thermochronology suggests sedimentary cover was fully eroded in the Neoproterozoic between ca. 720 to  $\geq$  600 Ma
- Time-temperature inversions indicate  $\sim$ 4 km of erosion that contributed to the formation of the Great Unconformity in North America

---

Corresponding author: Kalin McDannell, [kmcdannell@bates.edu](mailto:kmcdannell@bates.edu)

**Abstract**

It has long been speculated that isolated Paleoproterozoic basins of northern Laurentia are remnants of a once contiguous sedimentary cover due to similarities in stratigraphy, paleocurrent directions, sediment provenance, and geochronological data. However, corroborating evidence for this ‘superbasin hypothesis’ has been lacking outside the footprints of the preserved basins. We present new zircon and apatite (U-Th)/He and fission-track thermochronology data and time-temperature inversions from metamorphic basement that support the previous existence of sedimentary cover over currently exposed shield regions, bridging the gap between preserved basin strata across a large expanse of northern Canada. Inversions also reveal a notably synchronous and relatively rapid cooling event consistent with deep erosional exhumation during supercontinent breakup and Snowball Earth glaciations. Our study provides a comprehensive dataset from the exposed craton in northern Canada that supports an originally more widespread Proterozoic basin and offers additional evidence of  $\sim 4.3 \pm 1.1$  km of Neoproterozoic erosional exhumation that played a role in the formation of the Great Unconformity surface across North America.

**1 Plain Language Summary**

This study offers new insights into the idea that ancient sedimentary basins in northern Canada were once connected. The research shows that much of northern Laurentia was once covered by several kilometers of sedimentary rock, which was mostly eroded millions of years ago during a time of global ice ages and the breakup of a supercontinent. This erosion helped form the Great Unconformity, an important geological boundary found across North America. The findings support large-scale sediment deposition and erosion across the continent and provide a better understanding of how Earth’s surface evolved during a critical period in its history.

**2 Introduction**

Laurentian North America contains some of Earth’s most ancient rocks and is regarded as a model of long-term tectonic stability. The preservation of widely separated Paleoproterozoic sedimentary basins in northern Canada attests to this stability, suggesting minimal denudation over billions of years (Fig. 1). The geologic history relevant to this study begins in the Paleoproterozoic (2500–1600 Ma) with the growth of Laurentia during the ca. 2000–1800 Ma Taltson-Thelon and Hudsonian orogenies and associated post-orogenic mag-

matism (Hoffman, 1988). Our study area encompasses the Churchill Province (Fig. 1), which includes the Rae and Hearne cratons (Pehrsson et al., 2013). Churchill Province structural domains cooled below 300 °C during episodic exhumation from lower-to-middle crustal depths between ca. 1900 Ma to < 1750 Ma (Flowers et al., 2008; Kellett et al., 2020; Regis et al., 2021). Deep crustal exhumation was followed by widespread basement exposure—reflected by a prominent weathering surface and lateritic paleoregolith that is preserved near and beneath many of the intracratonic basins (Gall, 1992; Gall & Donaldson, 2006). The causes, timing, and tempo of cratonic surface evolution between deposition of these sediments and the Cambrian is poorly understood.

We focus on the areas between the Athabasca, Thelon, Hornby Bay, and Elu basins (Fig. 1). These basins share similar stratigraphic ages and depositional facies (Fig. 2) and have been considered part of a putative superbasin (e.g., Fraser et al., 1970; Young, 1979; Gall & Donaldson, 2006; Rainbird et al., 2007; Hahn et al., 2013; Furlanetto et al., 2016; Rainbird & Davis, 2022). The ‘superbasin hypothesis’ proposes that a massive, long-lived basin accumulated extensive sedimentary deposits over hundreds of millions of years. In this hypothesis, the current intracratonic basin footprints across northern Laurentia represent the erosional remnants of this once larger basin. What the superbasin hypothesis does not address is when erosion occurred to separate the remnant basins.

The prevailing idea is that intracratonic basin formation began with failed rifting and subsidence, followed by burial under detritus shed from the Trans-Hudson Orogen (Fraser et al., 1970; Hahn et al., 2013; Rainbird & Davis, 2022). The remnant basins (Fig. 1) may have been initially contiguous, part of an expansive arenite sand sheet deposited over a broad region with locally thicker depocenters that formed in response to thermal subsidence following Laurentia’s consolidation (Ramaekers et al., 2007; Rainbird et al., 2003; Rainbird & Davis, 2007). The basins have generally been viewed as isolated “lakes of gravel and sand” separated by vast areas of limited accommodation space (Ramaekers et al., 2007). The sedimentary cover was originally thicker and more widespread than what remains today, but it was still less than foreland or continental margin basins (Jefferson et al., 2007). Sediment accumulation within the intracratonic sag basins probably reached ~3–6 km at most, depending on burial model and depocenter location (Rainbird et al., 2003; Chi et al., 2018).

The Thelon and Athabasca basins ( $\sim 1\text{--}2$  km preserved thickness) are the best studied examples due to their association with unconformity-hosted uranium deposits (Jefferson et al., 2007; Alexandre et al., 2009). The Hornby Bay (Rainbird & Davis, 2022) and Elu basins (Ielpi & Rainbird, 2015), as well as the more distal  $\sim 14$  km-thick Wernecke (Furlanetto et al., 2016) and  $\sim 6$  km-thick Muskwa basin (Ross et al., 2001) near the modern, western cratonic margin (Fig. 1B) are interpreted to preserve the medial and distal (respectively) parts of a westerly flowing, pan-Laurentian drainage system. It was proposed that clastic sediment input from the east dwindled over time, followed by marine transgression from the west and flooding of the craton by an epicontinental sea, leading to shallow-water carbonate deposition (Hahn et al., 2013). Geochronology and regional stratigraphic similarities (Figs. 1 and 2) indicate deposition occurred across the cratonic interior from ca. 1700 Ma to  $< 1540$  Ma ( $< 1440$  Ma Hornby Bay and Elu basins), possibly extending to ca. 1270 Ma at the time of Mackenzie Large Igneous Province (LIP) emplacement (Hahn et al., 2013; Furlanetto et al., 2016; Rainbird & Davis, 2022; Pehrsson et al., 2023). During the main phase of the Grenvillian orogeny ca. 1100–1000 Ma, craton-wide sediment transport and deposition are theorized (Young, 1979; Rainbird et al., 1992, 2012, 2017), although strata of Grenvillian age are not presently preserved within Laurentia’s interior (Rainbird et al., 2012, 2017). Neoproterozoic basins, including Amundsen, Bylot, Fury and Hecla (Fig. 1) are found along the northern continental margin in Canada (Rainbird et al., 1996; Greenman et al., 2021). We use the terms ‘cratonic interior’ or ‘shield’ to refer to the oldest central region of Laurentia characterized by the thickest continental lithosphere  $> 225$  km (Steinberger & Becker, 2018) and fast seismic velocity, whereas ‘cratonic margin’ is primarily used to denote the far western and northern areas of thinner, transitional lithosphere ( $< 225$  km) along the modern coastline extending into the Canadian Arctic Archipelago.

The Proterozoic sedimentary rocks across northern Canada comprise three unconformity-bounded sequences: Sequence A ( $\geq 1700\text{--}1070$  Ma), Sequence B (1070–720 Ma), and Sequence C (720–540 Ma) (Young, 1979; Rainbird et al., 1996, 2017, 2020). Sequence A is the only sedimentary package located on the interior of the shield (partially preserved), whereas Meso- to Neoproterozoic Sequences B and C are preserved closer to the continental margin (Fig 1). Sequence C includes Cryogenian (720–635 Ma) diamictites that support the Snowball Earth hypothesis (Hoffman et al., 2017). The best studied stratigraphic sections with radiometric age control are located in the Hornby Bay and Amundsen basins along the margin (Figs. 1C and 2). For example, Figure 1C shows Great Bear Supergroup (informal

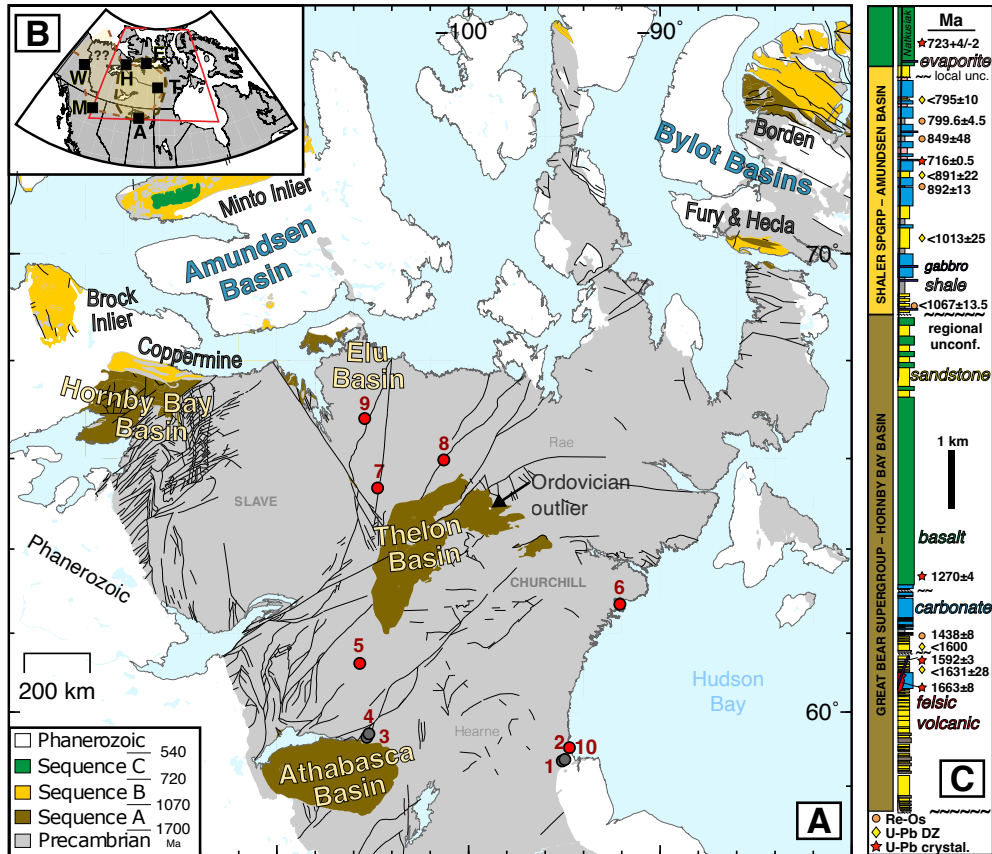


**Figure 1.** Location map of the northern Canadian Shield with simplified geology. Cratonic areas in gray are undifferentiated Precambrian basement, whereas areas in white are Phanerozoic (mostly Paleozoic) strata. Thin lines are regional faults. (A) Thermochronologic sample locations with respect to Paleoproterozoic basins. [1] 97-10-481; [2] 97-10-499; [3] 02-123A; [4] 00-196B/C; [5] 16EM1207A; [6] CL134; [7] 14NK-M044A04; [8] 12NK-L015; [9] 16BLB-R118A; [10] 97-10-365. Dark gray sample location points are previously published. Note that the age ranges for Sequences A–C are generalized and not necessarily representative of the preserved rocks in each basin. (B) Inset of Canada showing Paleoproterozoic basin remnants believed to be part of an inferred superbasin. Abbreviations: A–Athabasca; T–Thelon; E–Elu; H–Hornby Bay; W–Wernecke Supergroup; M–Muskwa Assemblage. (C) Stratigraphic column modified from Rainbird et al. (2020) showing well preserved sections from the Hornby Bay and Amundsen basins with radiometric age control. Note: Uppermost Re–Os date reported date of  $761 \pm 41$  Ma from Rainbird et al. (2020) revised to  $799.6 \pm 4.5$  Ma (Shipman et al., 2024). Rock types are color-coded (sandstone = yellow; basalt = green; felsic volcanic = red; gabbro = purple; carbonate = blue; shale = gray; evaporite = pink).

name) sedimentation occurred from  $> 1650$  Ma through  $< 1270 \pm 4$  Ma (Sequence A), followed by unconformity formation at  $< 1270$  Ma to  $> 1080$  Ma (Rainbird et al., 2017, 2020), representing a hiatus of approximately 200 Myr above which Shaler Supergroup (Sequence B) deposition ensued from  $1067 \pm 14$  Ma to ca. 720 Ma in Amundsen Basin (Rainbird et al., 2020) (Fig. 1). The Franklin LIP volcanism occurred around 720–718 Ma, heralding the breakup of supercontinent Rodinia and the rapid onset of an icehouse climate by 717 Ma (Pu et al., 2022).

Other than regionally localized Cryogenian-Ediacaran rocks (e.g., Yukon to the west of our area; Macdonald et al., 2023), the sedimentary record is mostly missing between ca. 720–515 Ma (Fig. 1A)—the only Paleozoic rocks identified on the craton in our study area are in the Hornby Bay (Rainbird & Davis, 2022) and Elu basins (Ielpi & Rainbird, 2015) and isolated Ordovician outliers near Thelon Basin (Bolton & Nowlan, 1979). The Hudson Platform hosts mostly Ordovician through Devonian strata (minor Mesozoic) (Sloss, 1963, 1988; Allen & Armitage, 2011; Lavoie et al., 2019; McDannell, Pinet, & Issler, 2022), whereas Paleozoic–Mesozoic rocks of the Western Canada Basin adjoin the Athabasca Basin further to the southwest (Fig. 1A).

Direct physical evidence to support the superbasin hypothesis is lacking over the shield areas exposed between the remnant inliers. Presently, the hypothesis draws support from various datasets, including geochronological, paleogeographic, and sedimentological data. However, the subsequent late Meso- to Neoproterozoic rock record is conspicuously absent within interior Laurentia, necessitating more speculative interpretation. Rainbird and Davis (2022) suggested that slow uplift and erosion removed the thinner deposits found between depocenters, where subsidence was more pronounced, effectively isolating the basins from each other. This hypothesis assumes a gradual erosion process resulting from the craton’s long-term uplift. However, the timing, scale, and extent of burial and erosion across Laurentia during the Proterozoic eon are still not fully understood, making this argument difficult to assess. This study explores hypotheses about the connectivity of the Proterozoic basins and investigates the potential timing and cause of the presumed superbasin’s erosional segmentation by leveraging thermochronological proxies for burial and erosion.

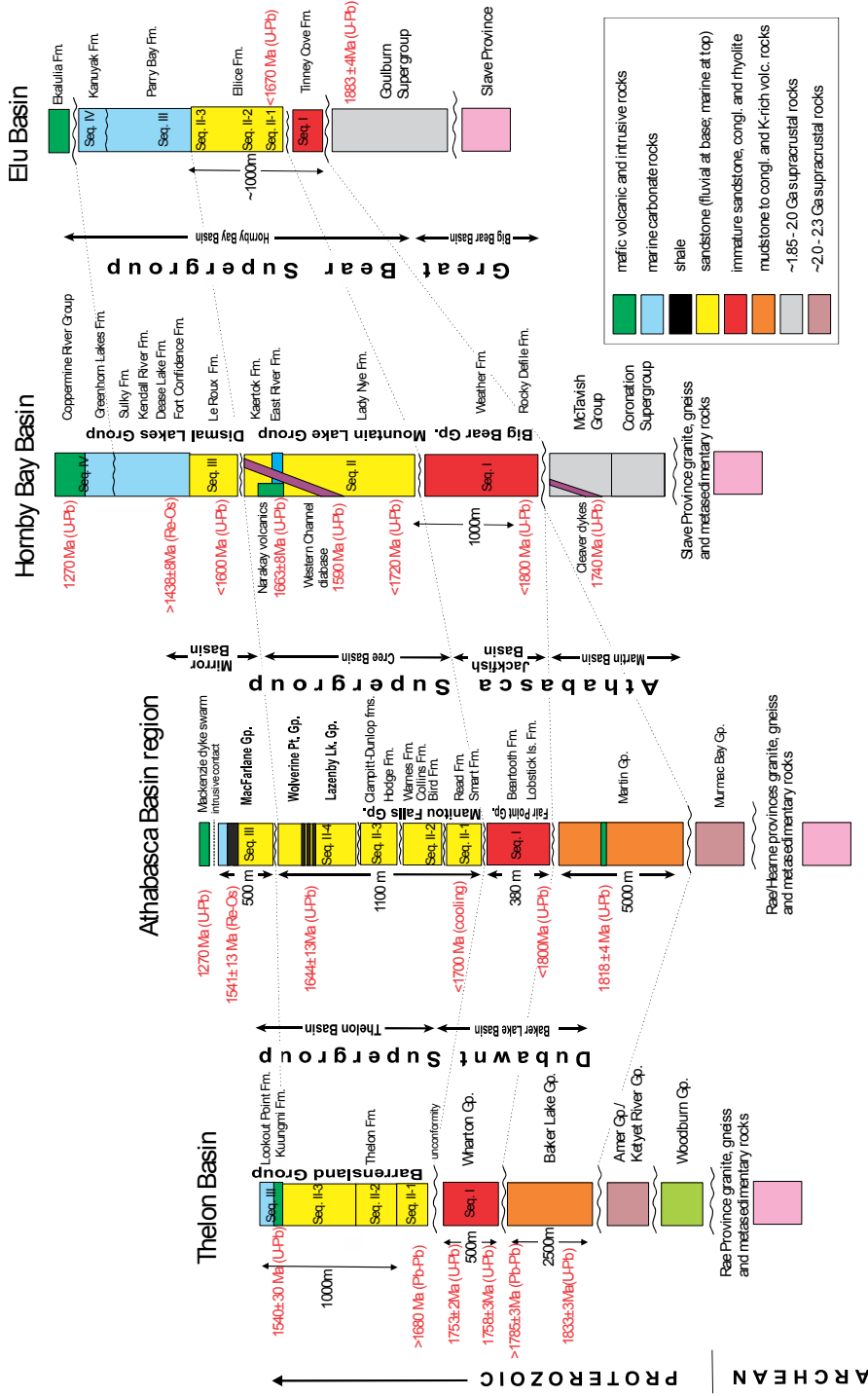


**Figure 2.** Regional sequence stratigraphic correlation of late Paleoproterozoic cratonic basins of northern Canada highlighting current geochronological constraints. Onset of deposition was approximately ca. 1750–1690 Ma in Thelon Basin (Davis et al., 2011), ca. 1740–1650 Ma in Athabasca Basin (Rainbird et al., 2007), < 1800 Ma to > 1670 Ma in Hornby Bay Basin (Rainbird & Davis, 2022), and > 1630 Ma in the Elu Basin (Ielpi & Rainbird, 2015). Basins are characterized by initial fill of rift-related, immature clastic rocks (immature sandstone, mudrocks and conglomerate) +/- volcanic rocks (Sequence I) followed by mainly fluvial +/- aeolian sandstone (Sequence II), marine sandstone and conformably overlying carbonate rocks (Sequence III) and marine carbonate and conformably overlying flood basalts (Sequence IV). Great Bear Supergroup is an informal term. Refer to the Supplementary Information for complete reference list for the regional stratigraphy and geochronology.



### 3 Methodology

Thermochronology is used to determine the timing of thermal events in a rock's history by measuring the temperature-dependent accumulation or loss of radiogenic isotopes (or their products) in minerals. The zircon and apatite (U-Th)/He methods (ZHe and AHe) measure the accumulation of helium produced by the radioactive decay of uranium, thorium, and samarium at temperatures spanning  $\sim 180\text{--}30$  °C for both methods (Reiners et al., 2017, for summary). Radiation damage modulates helium diffusivity in apatite and zircon depending on the accumulated lattice damage over time, which is a function of a sample's U and Th content and time-temperature ( $t$ - $T$ ) history (e.g., Flowers et al., 2009; Guenther et al., 2013). Similarly, the apatite fission track (AFT) method takes advantage of damage trails formed by the spontaneous fission of uranium that are sensitive to thermal annealing between temperatures of  $\sim 120\text{--}60$  °C (e.g., Green et al., 1985; Ketchum et al., 1999). These fission tracks are etched and counted across a polished grain area to determine the time over which tracks have accumulated. Fission-track lengths are highly sensitive to the style of thermal history because their formation and retention are influenced by both the peak temperature and the rate of cooling or heating. Together, these techniques reveal the timing and rates of thermal evolution in the Earth's upper crust, which can be linked to processes such as burial, erosion, and magmatism.

#### 3.1 (U-Th)/He Dating

Zircon and apatite underwent contracted (U-Th)/He analysis at the University of Colorado and the University of Calgary. The analytical protocol for (U-Th)/He data generated at the University of Colorado (apatite) are described in full in the *Supplemental Information* (SI). The University of Calgary (U-Th)/He analytical procedures (zircon) are similar and thoroughly described in McKay et al. (2021). The  $\alpha$ -ejection-corrected (U-Th)/He data are plotted and discussed in the text for more intuitive visual comparison to thermal histories (see below).

#### 3.2 Apatite Fission-Track Dating

Double dating by GeoSep Services was carried out using the laser ablation inductively coupled plasma mass spectrometry (LA-ICP-MS) U-Pb and modified- $\zeta$  apatite fission track methods (Cogné et al., 2020) with the same analytical procedures discussed in McDannell,

Pinet, and Issler (2022). Fission-track ages were determined using the laser ablation inductively coupled plasma-mass spectroscopy (LA-ICP-MS) method using the Washington State University (WSU) Finnigan Element II Magnetic Sector ICP-MS. The U-Pb apatite data are mainly characterized by Paleoproterozoic dates related to metamorphism and are thus decoupled from the low-temperature thermochronometers and are not discussed further. Detailed electron microprobe elemental data were obtained for the analysed grains to calculate the AFT kinetic parameter  $r_{mr0}$  to aid in interpretation and modeling. The  $r_{mr0}$  parameter describes the relative reduction in fission-track length due to differential thermal annealing in different apatite compositions (Carlson et al., 1999). More detailed methods are in the SI.

## 4 Results

### 4.1 Deep-Time Thermochronology of the Northern Canadian Shield

To quantitatively examine the erosion and burial record across the craton, rock samples from exposed Churchill Province basement (Fig. 1) were dated by multiple thermochronological methods, which is critical for elucidating deep geologic time (McDannell & Flowers, 2020). We also compiled data from previously published examples (Fig. 1). We describe all previously published data and our new analytical results for each sample (Fig. 3). Only combined data for locations 1–2 and 3–4 are previously published (Flowers, 2009; McDannell & Keller, 2022), whereas samples 5–10 are new data presented here (Figs. 1 and 3). The analytical data tables are provided in the SI Appendix (Data S1) along with detailed analytical methodology.

#### 4.1.1 Samples 1–2: 97-10-481, 97-10-499 — ZHe, AFT, and AHe

Samples 97-10-481 and 97-10-499 were collected from Archean basement rocks, a hornblende granite and foliated granodiorite, respectively, in the Seal River region of the Hearne craton near the southwest Hudson Bay margin (Fig. 1). The ZHe, AFT, and AHe data for these samples were published in McDannell and Keller (2022). The samples are < 10 km from one another and a few kilometers from the nonconformable basement contact with Ordovician carbonate rocks that are ca. 470–450 Ma in age across the Hudson Platform. The zircon grains exhibit a negative date-effective uranium trend ( $eU = U + 0.238 \times Th + 0.0012 \times Sm$ ), and  $\alpha$ -ejection corrected dates span ca. 700 Ma to 1 Ma ( $n =$

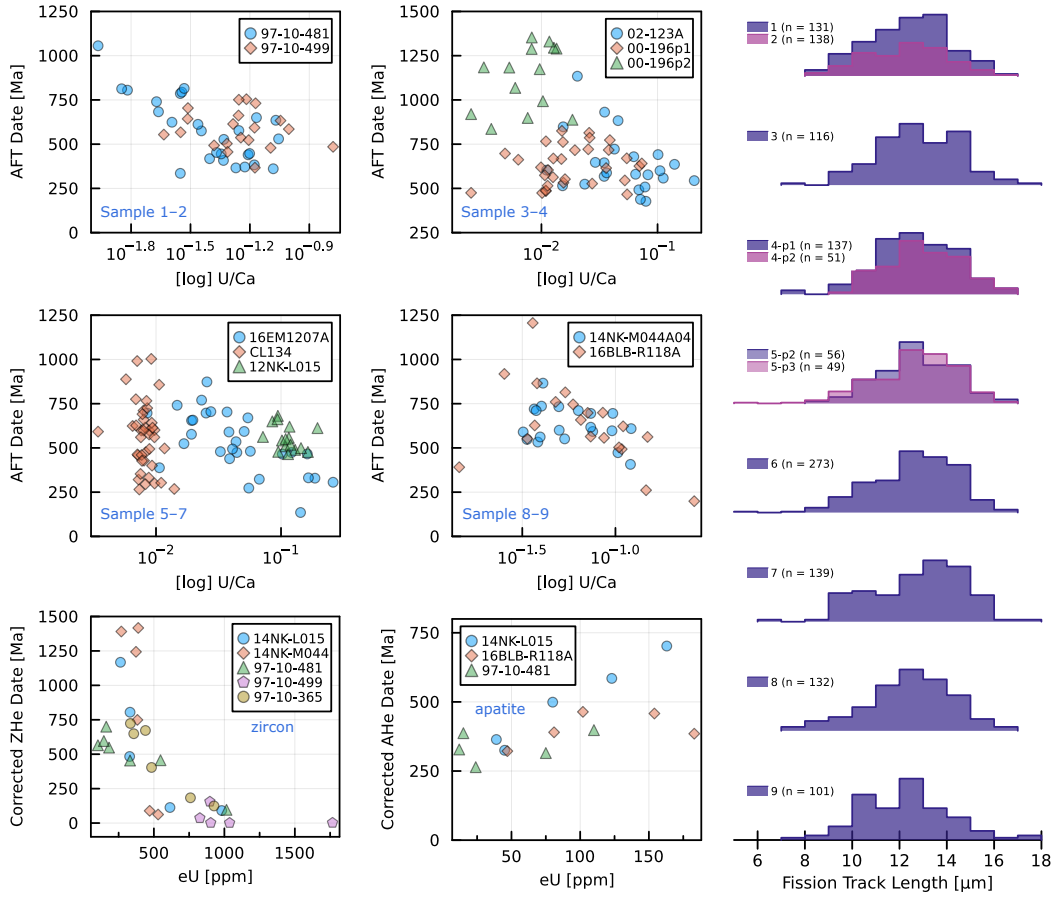


**Figure 3.** New and previously published thermochronological data including LA-ICP-MS apatite fission track data with measured conventional track-length distributions (without c-axis projection) and zircon and apatite (U-Th)/He dates for exposed Precambrian basement samples from northern Laurentia. All sample numbers (1–10) refer to the same numbers as Fig. 1 and Fig. 6. The -p1, -p2, -p3 suffix for track lengths refers to kinetic populations 1, 2, and 3, respectively for the corresponding sample. U/Ca is the uranium concentration obtained by the ratio of  $^{238}\text{U}$  to  $^{43}\text{Ca}$  during LA-ICP-MS measurement. Alpha-ejection correction of raw analytical (U-Th)/He dates is a consequence of the energetic stopping distances primarily associated with the  $^{238}\text{U}$ ,  $^{235}\text{U}$ , and  $^{232}\text{Th}$   $\alpha$ -decay chains that cause  $^4\text{He}$  loss from zircon and apatite crystals.

12) and eU values of  $\sim 100$ – $1765$  ppm. Apatite (U-Th)/He dates for 97-10-481 range from ca. 400–265 Ma ( $n = 5$ ) and eU values of  $\sim 15$ – $110$  ppm. The AFT data from both samples were merged since they are statistically indistinguishable with similar fission-track annealing kinetics typical of near-endmember fluorapatite ( $r_{mr0} \sim 0.86$ – $0.82$ ; mean = 0.84). The combined AFT data produced a central age of  $563 \pm 21$  Ma ( $n = 47$ ) and a conventional mean track length (MTL) of  $12.34 \pm 1.7$   $\mu\text{m}$  ( $n = 269$ ).

#### **4.1.2 Sample 3: 02-123A — $^{40}\text{Ar}/^{39}\text{Ar}$ , ZHe, AFT, & AHe**

This thermochronologic sample suite comes from a vein in felsic gneiss basement of the Chipman tectonic domain in the Athabasca Basin near the Snowbird Tectonic Zone. The integrated datasets were discussed in previous publications (e.g., McDannell & Flowers, 2020; McDannell, Keller, et al., 2022b) and include a high-temperature constraint in the form of a K-feldspar multi-diffusion domain  $^{40}\text{Ar}/^{39}\text{Ar}$  spectrum with step ages spanning ca. 1765–1670 Ma, with a pattern of  $^{39}\text{Ar}$  release indicative of rapid cooling from  $> 300$  °C (McDannell, Zeitler, & Schneider, 2018). The AFT and AHe data for sample 02-123A were published by Flowers (2009). Two corrected, low eU ( $< 20$  ppm) ZHe dates are ca. 1300 Ma and 1400 Ma from nearby sample 00-196C and AHe dates for 00-123A range from 650–450 Ma ( $n = 7$ ) across 37–53 ppm eU. The AFT central age is  $660 \pm 45$  Ma ( $n = 25$ ) with an unprojected MTL of  $12.94 \pm 1.65$   $\mu\text{m}$  ( $n = 116$ ) characterized by fluorapatite annealing kinetics (mean  $r_{mr0}$  value of 0.83 and  $D_{par}$  of 1.81  $\mu\text{m}$ ). The  $t$ - $T$  model shown below is the same model from McDannell, Keller, et al. (2022b).

#### **4.1.3 Sample 4: 00-196B & 00-196C — ZHe, Multikinetic AFT, & AHe**

Thermochronometric data for samples 00-196B and 00-196C were reported by Flowers et al. (2006) from the southwestern Chipman domain near Athabasca Basin. Each sample is from the same location and 00-196B is a tonalitic gneiss that hosts a cross-cutting migmatitic mafic dyke that 00-196C was collected from in exposed outcrop. A robust collection of ZHe, multikinetic AFT (e.g., Issler et al., 2022), and AHe data exist for this location but have never been fully integrated prior to this contribution. The uncorrected ZHe dates from the Chipman domain range from 1700–1300 Ma ( $n = 8$ ) and are all low eU with values between  $\sim 10$  to  $< 100$  ppm, whereas the nine corrected AHe dates are low eU, between ca. 950–550 Ma. Each AHe date was modeled individually and the  $r_{mr0}$  value was allowed to vary around  $0.83 \pm 0.02$  (e.g., McDannell & Issler, 2021; McDannell & Keller, 2022). The

multikinetic AFT data are the most intriguing since the contrasting lithologies, which result in contrasting apatite compositions, yield pronounced differences in fission-track annealing behavior (refer to Issler et al., 2022 for multikinetic AFT interpretation scheme). Kinetic population one (i.e., 00196-p1 in Fig. 3) is mostly from the gneiss sample 00-196B and has an AFT central age of  $645 \pm 19$  Ma ( $n = 31$ ;  $p(\chi^2) = 0.27$ ), whereas the mafic dyke sample 00-196C has a central age of  $1217 \pm 80$  Ma ( $n = 17$ ;  $p(\chi^2) = 0.93$ ) calculated in IsoplotR (Vermeesch, 2018). The unprojected mean track lengths for each kinetic population are  $12.71 \pm 1.72$   $\mu\text{m}$  ( $n = 137$ ) and  $13.26 \pm 1.52$   $\mu\text{m}$  ( $n = 51$ ), respectively, and their mean  $r_{mr0}$  values are 0.824 ( $D_{par} = 1.99$   $\mu\text{m}$ ) and 0.798 ( $D_{par} = 2.32$   $\mu\text{m}$ ); with the lower  $r_{mr0}$  signifying higher track retentivity in the latter population due to elevated Cl and OH in the apatite anion site.

#### 4.1.4 *Sample 5: 16EM1207A — Multikinetic AFT*

Sample 16EM1207A was collected from a psammitic arenite in the Firedrake domain of the southern Rae craton (also named sample z11850). Regis et al. (2021) dated the sample by zircon and in situ monazite U-Pb methods yielding metamorphic ages of  $1852 \pm 16$  Ma and  $1836.2 \pm 2.7$  Ma ( $2\sigma$ ). 16EM1207A was dated here for AFT and it is multikinetic with three age populations related to differential annealing response between apatite compositional groups. The overall sample AFT central age is  $514 \pm 29$  Ma ( $n = 29$ ), excluding a single precise outlier grain age of  $135 \pm 20$  Ma that was retained for completeness during modeling but left out of the statistical reporting since it distorts the mixture modeling. Mixture modeling yields three peak ages for the sample of  $321 \pm 11$  Ma (grain proportion = 17%),  $478 \pm 16$  Ma (38%), and  $666 \pm 37$  Ma (44%). The interpreted kinetic population one AFT central age is  $320 \pm 11$  Ma ( $n = 5/6$ ;  $p(\chi^2) = 0.87$ ); population two is  $486 \pm 14$  Ma ( $n = 11$ ;  $p(\chi^2) = 0.49$ ); and population three is  $635 \pm 34$  Ma ( $n = 13$ ;  $p(\chi^2) = 0.09$ ), in general agreement with the mixture model peaks. The first population does not include track lengths, whereas population two contains 56 lengths with an unprojected MTL of  $12.85 \pm 1.44$   $\mu\text{m}$  and population three contains 49 lengths with a MTL of  $12.68 \pm 1.71$   $\mu\text{m}$ . The population grain-age kinetics yield average  $r_{mr0}$  and  $D_{par}$  values of 0.846 and 1.64  $\mu\text{m}$  (pop 1); 0.835 and 1.77  $\mu\text{m}$  (pop 2); 0.819 and 1.82  $\mu\text{m}$  (pop 3).

#### 4.1.5 *Sample 6: CL134 — AFT*

Sample CL134 was collected from a medium/coarse-grained gabbroic dyke in the Rankin Inlet greenstone belt of the Churchill-Hearne Province in the Meliadine Gold District (Lawley et al. (2016) sample 13LVA-04). The dyke is located at the Discovery Outcrop along Pyke Break where it cuts turbiditic host rocks, including a banded iron formation and the Sam Formation, and has a hydrothermal/metamorphic age of  $1807 \pm 18$  Ma (Lawley et al., 2016). CL134 is the only single thermochronometer sample presented herein but has abundant fission-track length data for better constraining thermal history style. The AFT central age is  $561 \pm 67$  Ma ( $n = 40$ ), and if a single precise  $299 \pm 80$  grain age is excluded, it passes the  $\chi^2$  test ( $p = 0.067$ ; central age is then  $580 \pm 61$  Ma). We nonetheless retained all the analytical data for inverse modeling. The unprojected MTL for CL134 is  $12.60 \pm 1.83$   $\mu\text{m}$  ( $n = 273$ ) and the apatites are characterized by elevated OH and Fe with a mean grain-age  $r_{mr0}$  value of 0.803 (lengths  $D_{par} = 2.24$   $\mu\text{m}$ ), implying enhanced track retentivity compared to common fluorapatite ( $r_{mr0} = 0.83$ ).

#### 4.1.6 *Sample 7: 14NK-M044A04 — ZHe and AFT*

Sample 14NK-M044A04 was collected from a ca. 2500 Ma intermediate quartz diorite (5–20% quartz) in the Queen Maud block of the northwestern Churchill-Rae craton near the boundary with the Thelon Tectonic Zone (GSC lab # z11408). Alpha-corrected ZHe dates span ca. 1415–60 Ma ( $n = 6$ ) and eU concentrations of 270–530 ppm. The AFT central age is  $620 \pm 24$  Ma ( $n = 20$ ) by IsoplotR analysis. Three precise outlier single-grain ages cause modest overdispersion (15%), but exclusion of those data does not meaningfully change the central age. The unprojected MTL is  $12.40 \pm 1.76$   $\mu\text{m}$  ( $n = 132$ ) and the mean  $r_{mr0}$  annealing kinetic parameter is 0.816 ( $D_{par} = 2.00$   $\mu\text{m}$ ).

#### 4.1.7 *Sample 8: 12NK-L015 — ZHe, AFT, and AHe*

Sample 12NK-L015 was collected from an exposed well foliated, clinopyroxene-hornblende quartz diorite gneiss that crystallized at  $2513.6 \pm 3.2$  Ma in the Queen Maud block of the northern Churchill-Rae craton (Davis et al., 2014). The corrected ZHe dates are ca. 1170–90 Ma ( $n = 5$ ) with eU values spanning 260–980 ppm. The AFT central age is  $551 \pm 17$  Ma ( $n = 16$ , 10% dispersion). The unprojected MTL is  $12.78 \pm 1.96$   $\mu\text{m}$  ( $n = 139$ ) and the mean  $r_{mr0}$  annealing kinetic parameter is 0.832 ( $D_{par} = 1.90$   $\mu\text{m}$ ). Apatite He dates span

ca. 40–163 ppm eU and range in age from approximately 325–700 Ma. Each AHe date was modeled individually and the  $r_{mr0}$  value was allowed to vary ( $0.83 \pm 0.01$ ; see below).

#### **4.1.8 Sample 9: 16BLB-R118A — AFT and AHe**

Sample 16BLB-R118A is a foliated hornblende-biotite quartz diorite from the Overby Lake domain at the Slave craton boundary with the 1.9 Ga Thelon Tectonic Zone. Hornblende and biotite  $^{40}\text{Ar}/^{39}\text{Ar}$  data for this sample are reported in Camacho et al. (Camacho et al., 2020). The hornblende  $^{40}\text{Ar}/^{39}\text{Ar}$  date is  $1896 \pm 18$  Ma (low confidence) and the biotite age spectrum is discordant but yields a similar ca. 1900 Ma date. Both systems were presumably disturbed by metamorphic overprinting. The AFT central age is  $596 \pm 53$  Ma ( $n = 20$ ) and the conventional MTL is  $12.23 \pm 1.81$   $\mu\text{m}$  ( $n = 101$ ). 16BLB-R118A is typified by a mean  $r_{mr0}$  of 0.812 and mean  $D_{par} = 2.37$   $\mu\text{m}$ . Corrected AHe dates fall in a narrow range between ca. 320–465 Ma ( $n = 5$ ; 47–183 ppm eU). Each AHe date was modeled individually and the  $r_{mr0}$  value was allowed to vary ( $0.83 \pm 0.01$ ).

#### **4.1.9 Sample 10: 97-10-365 — ZHe**

Sample 97-10-365 is a foliated Archean granodiorite in the Hearne domain near the southwest Hudson Bay margin, only 40 km north of Samples 1–2 from the mouth of the Seal River. This samples includes only ZHe data with  $\alpha$ -corrected dates ranging from ca. 725 Ma to 125 Ma across  $\sim 330$ –930 ppm eU. We note that there does not appear to be any direct spatial association of these samples (i.e., 1, 2, and 10) with regional, possibly reactivated fault structures, nor coincidence with younger dykes, with the only known regional dykes being the 1267 Ma Mackenzie dike swarm.

## **5 Thermal History Modeling Approach**

Understanding the nuances of deep-time thermal history modeling is essential for accurately constraining geological processes, as these models provide the foundational framework for interpretation. We go over some of these topics before discussing our results. The main priorities to consider for modeling are the thermochronometer dates, sources of uncertainty, and the incorporation of reliable geologic information. Deep-time thermal histories in particular require large datasets to increase  $t$ – $T$  resolution and reduce nonuniqueness (McDannell & Flowers, 2020); uncertainties in diffusion/annealing kinetic models, limited

resolving power across deep time, and prior model assumptions may all contribute to variability in thermal history predictions with respect to measured data.

### 5.1 Kinetic Model Uncertainties

The relative kinetic compatibility between high and low-temperature thermochronometric systems ( $^{40}\text{Ar}/^{39}\text{Ar}$ , ZHe, AFT, AHe) may lead to particularly intractable problems for thermal history modeling that are not easily dealt with (i.e., misfit between predicted and observed data). An important point is that due to uncertainty, deep-time modeling using only a single thermochronometer is perilous—with  $t$ - $T$  results increasingly becoming more reliant on assumptions than constrained by data over longer timescales. This limitation arises not from inherent flaws in the techniques but rather from a lack of available data or complementary information, such as independent constraints on diffusion/annealing kinetics, geological context, or additional thermochronometric systems that could help constrain the thermal history.

Our discussion focuses primarily on the (U-Th)/He systems, which are not as well calibrated empirically compared to the fission-track method, and utilize fission-track annealing kinetics as a general proxy for  $\alpha$ -radiation damage annealing (e.g., Flowers et al., 2009; Guenther et al., 2013). We use the ZHe chronometer as an example to explore sources of methodological uncertainty with respect to  $t$ - $T$  modeling. The zircon radiation damage accumulation and annealing model (ZRDAAM) suggests that He retentivity varies with radiation dose, initially increasing with  $\alpha$ -recoil damage to reach a closure temperature of approximately 180 °C, before decreasing sharply at higher doses, likely due to enhanced connectivity between damage zones (Guenther et al., 2013). The high-damage end of the ZRDAAM model where ‘rollover’ to higher diffusivity occurs—and where measured and predicted age discrepancies usually arise—is less well constrained due to a lack of experimental data (e.g., Anderson et al., 2017). Studies suggest this change in diffusivity probably transpires at a lower damage threshold than is implemented in the current model (Powell et al., 2016; Gautheron et al., 2020; Guenther, 2021).

An apparent issue relevant for deep-time applications is that kinetic models (such as the ZRDAAM) do not allow uncertainties in the damage annealing function to be accounted for during modeling (cf. J. Stephenson et al., 2006). This is not unique to the ZHe method and is a result of the fact that experimentally derived kinetic variability is poorly known



(i.e., is radiation damage in zircon best described by fission track or  $\alpha$ -recoil annealing; see Guenther, 2021). This can be crudely accounted for in the AHe damage model of Flowers et al. (2009) by changing the  $r_{mr0}$  value controlling fission-track annealing resistance—but this assumes that: [i]  $r_{mr0}$  is independently known from elemental analysis; [ii] apatite chemistry appreciably affects He diffusion (e.g., Gautheron et al., 2013); and [iii] the physics governing fission-track annealing adequately describe  $\alpha$ -damage annealing (Flowers et al., 2009). However, elemental data are rarely collected or published, and the details of He diffusion systematics in slowly cooled apatite are possibly less understood than in zircon (McDannell, Zeitler, Janes, et al., 2018; Guo et al., 2024).

## 5.2 Apparent Age Uncertainties

Total (U-Th)/He date uncertainties exceed analytical error and are poorly constrained (Flowers et al., 2023). Numerous sources of ‘geological’ age dispersion and uncertainties in kinetic models impede a full accounting of the total uncertainties required for modeling; thus necessitating different strategies for dealing with uncertainty. The best strategy is to acknowledge uncertainty and address it in an unbiased manner, while being mindful that at a certain point the misfit between the data and model may be unreasonably large—still making critical evaluation of misfit difficult when we don’t know what the total uncertainties should be. In spite of this, the expectation that integrated (high  $n$ ) datasets across multiple thermochronometric systems should be reproduced ‘perfectly’ within inversions is unrealistic considering the imperfect kinetic calibrations that underpin predictive model capabilities (both within and between methods), as well as the geological complexity that is potentially unaccounted for in deep time. Currently, the only available approach is to implicitly convolve uncertainties from analytical data (e.g., isotopic zonation, grain morphology,  $\alpha$ -ejection) with unquantified kinetic uncertainties into a single uncertainty associated with the modeled date—which, within this scheme, assuredly results in an overall total uncertainty that is underestimated. To address this issue, future advancements should aim to directly incorporate laboratory experimental data that better constrain kinetic variability and separate analytical date uncertainty from kinetic model uncertainty.

One procedure used here for handling date uncertainty is to treat thermochronometer age errors or kinetic proxy variability (AFT and AHe only) as unknown parameters within a Bayesian framework and allow them to be sampled iteratively within an inversion by rescaling the data errors (e.g., 1–100 $\times$  the input ZHe error; Gallagher, 2012) or resampling the

kinetics assuming a normal distribution centered on the mean. This approach acknowledges that while the measured date or kinetic proxy is known, the associated uncertainty is poorly known. To provide additional context and illustrate age scatter we discuss ZHe dates from a few of our samples. A ZHe date-eU trend can be very sensitive to, and indicative of, specific  $t$ - $T$  conditions (e.g., Ault et al., 2018). For example, our zircon dataset for Samples 1–2 is limited, but it displays a relatively clear date-eU trend (Fig. 3). However, there are gaps in the eU trend, specifically between  $\sim 600$ – $800$  ppm and  $1100$ – $1700$  ppm, where no data are available. The latter gap is less concerning as dates approach zero around  $1000$  ppm. While the date-eU trend may appear straightforward, larger datasets containing  $15$ – $20$  or more grains often reveal age dispersion across the eU spectrum (e.g., McDannell, Keller, et al., 2022b; Thurston et al., 2024). Small ZHe datasets with only a few grains isolated in eU space typically lack sufficient  $t$ - $T$  sensitivity for modeling—allowing nearly any thermal history to explain the data (e.g., Peak et al., 2023).

With the inclusion of data from Sample 10 with Samples 1–2, the mean analytical uncertainty associated with the uncorrected ZHe dates is  $\sim 2.5\%$  ( $1\sigma$ ). On the other hand, Empirical Bayesian estimation of the total uncertainty is derived from the scatter in the data (e.g., McDannell, Keller, et al., 2022b), calculated by considering the standard deviation of the ages and their associated uncertainties weighted by a Gaussian kernel in eU space ( $\sigma_{\text{eU}} = 100$  ppm). The underlying assumption is that grains with similar eU values should exhibit similar ages within a given eU range. The total uncertainty was then estimated based on the observed dispersion within each eU interval and was found to be on the order of  $\sim 20$ – $30\%$ , or up to  $60\%$  or more for individual dates across both the uncorrected and  $\alpha$ -corrected date-eU trend. This level of uncertainty highlights the challenges of interpreting small datasets and sources of error in deep-time studies, emphasizing the need for larger or complementary thermochronometric data to constrain thermal histories more robustly.

### 5.3 Modeling Philosophy

Despite employing Bayesian inversion methods in this study (e.g., Gallagher, 2012, 2023), it is important to address the Frequentist modeling approach, which remains widely used in thermochronology. In principle, both Bayesian and Frequentist statistics offer valid approaches to thermochronology, however the latter methodology has fundamental drawbacks that make it less suited for deep-time problems. Inverse modeling using the commonly adopted HeFTy software (Ketcham, 2005) produces  $t$ - $T$  results that are visually intuitive

due to the use of formal goodness-of-fit (GOF) statistics ( $p$  values) to evaluate model predictions against observational data. However, these statistical tests rely on the *critical* assumption that the data uncertainties and the kinetic models governing diffusion and annealing are accurately known and well estimated—an assumption that, as previously mentioned, is widely recognized as flawed.

Thermal history resolution theoretically improves with the inclusion of more data in Bayesian inversions, whereas the statistical framework of Frequentist-based modeling fails when applied to large or highly precise datasets (Vermeesch & Tian, 2014)—an obvious shortcoming for deep-time applications that crucially rely on the analysis of large datasets. To circumvent these issues, ad hoc data averaging, a priori inflation of uncertainties, adjustment of minimum GOF statistics, and data culling (e.g., removal of high-eU zircons) are routinely employed to reduce dataset precision and size and to relax statistical rigor in an effort to obtain acceptable  $t$ - $T$  results, thereby introducing considerable bias and subjectivity into the modeling process (McDannell, Keller, et al., 2022a, for discussion). Collectively, these issues present significant limitations because if the underlying uncertainties, kinetic parameters, or geologic constraints are mischaracterized, the resulting thermal histories may appear statistically robust while failing to reflect actual geological processes or events, undermining model reliability. Bayesian methods explicitly incorporate these uncertainties into the modeling framework, systematically addressing them through probabilistic inference rather than relying on ad hoc data modification to satisfy statistical tests, resulting in a more transparent process; one that may nonetheless result in misfits between observations and predictions, but should be used to further probe thermochronometric system behavior.

We utilized an exploratory  $t$ - $T$  modeling approach that enables the investigation of a wide range of potential thermal histories that honor geologic information and provide greater flexibility in understanding complex natural processes. Our modeling philosophy is centered on embracing probabilistic reasoning to integrate thermochronometric data, prior geologic knowledge, and uncertainty into a cohesive framework. We can then assess how our data constrain key history parameters by identifying fits to observed data and heuristically refine our priors or collect additional data if necessary (e.g., McDannell, O’Sullivan, et al., 2022). For deep time problems, the latter step can be notoriously difficult due to a lack of tangible information to guide further modeling (e.g., additional thermochronologic data will not resolve [relative] kinetic model miscalibrations). In contrast to our perspective, inverse thermal history models are sometimes intended as ‘hypothesis tests’ for geologic scenarios

in deep time, however, the conclusions drawn from such tests (e.g., Flowers et al., 2020) are often “too vague to fail” (Cleland, 2013)—highlighting the difficulty of robustly evaluating hypotheses framed as falsifiable predictions in earth science.

## 6 Thermal History Modeling Results

In this paper, forward models serve as a comparative tool to explore different  $t$ – $T$  scenarios and build intuition about the types of thermal histories that generate distinct thermochronologic data trends, whereas inverse models are used to evaluate the level of confidence in a specific interpretation.

### 6.1 Forward Modeling

We first tested several scenarios by focusing mostly on the ZHe and AFT systems since, based on our results, those data have the most constraining power in the Proterozoic. For a given thermal history, eU (radiation damage proxy) and grain size are the respective primary and secondary controls on (U-Th)/He dates, whereas apatite composition and style/rate of cooling govern AFT population ages and track-length distributions. Therefore, closer inspection of our data with respect to general date-eU trends, grain size, and  $t$ – $T$  relationships provide context for further modeling (Fig. 3).

1. Zircon grain sizes are consistent across all samples with a mean equivalent spherical radius of  $51 \pm 2 \mu\text{m}$  ( $\sigma_m$ ,  $n=29$ ). Refer to data tables in the Supplementary Information.
2. In detail, the combined ZHe data from Samples 1, 2, and 10 and Samples 7–8 have divergent  $\alpha$ -corrected date-eU trends at low-to-moderate eU concentrations (Fig. 3; see below). The age difference at low eU could also be related to larger, more He retentive grains for the northern samples but that is ruled out due to point #1 above.
3. The AFT method is the best empirically calibrated thermochronometer available (e.g., Laslett et al., 1987; Carlson et al., 1999; Ketchum et al., 1999). Our fission-track central ages are mostly around 650 Ma, with a few examples being ca. 600–500 Ma. The younger central age samples are generally lower retentivity with  $r_{mr0}$  values around 0.83 to 0.84 indicative of common fluorapatite. The older AFT data are characterized by  $r_{mr0}$  values of  $\sim 0.80$  to 0.81, signifying higher retentivity, and are therefore unlikely to be reset by potentially minor heating events typical for

the shield in the Phanerozoic. The older AFT data have a greater likelihood of constraining primary cooling through 120 °C that, based on the ages, occurred in the Neoproterozoic.

4. The AHe dates are mostly Paleozoic in age, suggesting resetting by thermal events in the Phanerozoic. The northerly samples #8–9 have a few high-eU, > 100–160 ppm grains spanning ages of ca. 700–465 Ma, respectively. High-eU apatite grains are often rare in AHe datasets but are more retentive and contain the most information constraining cooling from temperatures of < 100 °C (McDannell & Keller, 2022, see supplementary discussion).

The purpose of our forward models is to get a general sense of what thermal history properties may be necessary to explain the data and are only snapshots of the many, potentially more complex histories that could explain the data. We used the published inversions for Samples 1–3 (McDannell, Keller, et al., 2022b; McDannell & Keller, 2022) as guides for forward modeling tests. Synthetic ZHe dates were generated from input  $t$ - $T$  paths (Fig. 4) using the ZRDAAM across 0–2000 ppm eU (100 ppm increment) with a fixed 50  $\mu$ m grain radius that reflects our dataset mean. Analyzed ZHe data are plotted for comparison, with 20% uncertainty, which is the median of our previously mentioned Empirical Bayes error estimate.

To first order, low-eU, older grains contain the most information about the conditions of thermal resetting in the Proterozoic, whereas younger, moderate-to-high eU zircons constrain Phanerozoic conditions (Fig. 4). Alpha-corrected low-eU ZHe dates range from < 1500 to 600 Ma and AFT central ages are between ca. 650 and 550 Ma (Fig. 3). These thermochronometric dates alone require a general heating-to-cooling trajectory, regardless of supporting geologic information (see Section 6.4 on interpretation). The ZHe dates between  $\sim$ 250–400 ppm eU for the older northerly samples (#7–8) imply a lower overall Mesoproterozoic maximum heating magnitude of  $\sim$ 150 °C and either a different Phanerozoic thermal history or a similar one at higher temperatures. The rocks next to Hudson Bay (#1–2, 10) presumably reached higher temperatures > 150–190 °C some time after 750 Ma to fully reset the low-eU zircons (Fig. 4A–B), whereas the moderate-eU ZHe dates at 800–1000 ppm also require Phanerozoic heating (Fig. 4C–D).

Forward models indicate that if the basement was fully exhumed and remained so for the majority of the Proterozoic—the predicted ZHe dates would be much too old com-

pared to our observed data—thereby requiring some Mesoproterozoic heating followed by Neoproterozoic cooling (Fig. 4A–B). Another possible explanation is that the  $< 1700$  Ma thermochronometric ages of all samples reflects Neoproterozoic exhumation of the basement alone, without the need for a thick sedimentary package above. However, the regional stratigraphic relationships (Fig. 2) and studies of Laurentian cratonic exhumation demonstrate that initial basement unroofing to the surface occurred broadly in the Paleoproterozoic (e.g., Flowers et al., 2006; Rainbird et al., 2007; Flowers, 2009; Davis et al., 2011; McDannell, Zeitler, & Schneider, 2018; Regis et al., 2021). Thus it is highly improbable that crustal exhumation [of discrete tectonic domains between the remnant basins] stalled in the mid-crust for up to 1000 Myr before resuming in the Neoproterozoic (see Section 6.2 below).

We also looked into two possibilities for late Neoproterozoic exhumation of the Canadian Shield (Fig. 4E–F)—cooling during the Cryogenian (McDannell, Keller, et al., 2022b; McDannell & Keller, 2022) and later post-Ediacaran cooling (Peak et al., 2023). A late Neoproterozoic cooling from 500–475 Ma over 170–20 °C produces agreement across the younger, low date-eU trend, but misses the older zircons, whereas the cooling path from 690–600 Ma over 170–20 °C better matches the oldest zircons but misses the other low-eU grains (Fig. 4E–F). In this instance, it becomes very clear that the date itself, and the absolute and relative uncertainties for individual dates, can highly influence whether specific  $t$ - $T$  solutions are accepted by the modeling software during inversion. Furthermore, if the date-eU trend is also changed by ad hoc data averaging, then it is inevitable that  $t$ - $T$  sensitivity will be lost and a greater range of permissible  $t$ - $T$  paths will be allowed (i.e., the “too vague too fail” problem).

We can then examine the AFT data, where rapid cooling through 100 °C at either 650 or 500 Ma would yield AFT ages nearly equivalent to those cooling times if there were no subsequent Phanerozoic reheating events. Consequently, the AFT data must either be retentive enough to withstand minor reheating (without totally resetting during burial), or indicate that some degree of Phanerozoic reheating took place. The younger AHe data suggest later reheating is likely. Phanerozoic surface histories across the exposed Canadian Shield are reasonably well-documented, exhibiting at least one thermal peak reflecting Paleozoic burial (typically  $< 120$  °C) and sometimes a minor, late Mesozoic burial event  $< 75$  °C (e.g., Crowley, 1991; Osadetz et al., 2002; Kohn et al., 2005; Feinstein et al., 2009; Flowers, 2009; McDannell et al., 2019; McDannell, Pinet, & Issler, 2022; McDannell & Keller, 2022). Paleozoic and Mesozoic rocks, mostly Ordovician through late Devonian and Cretaceous in

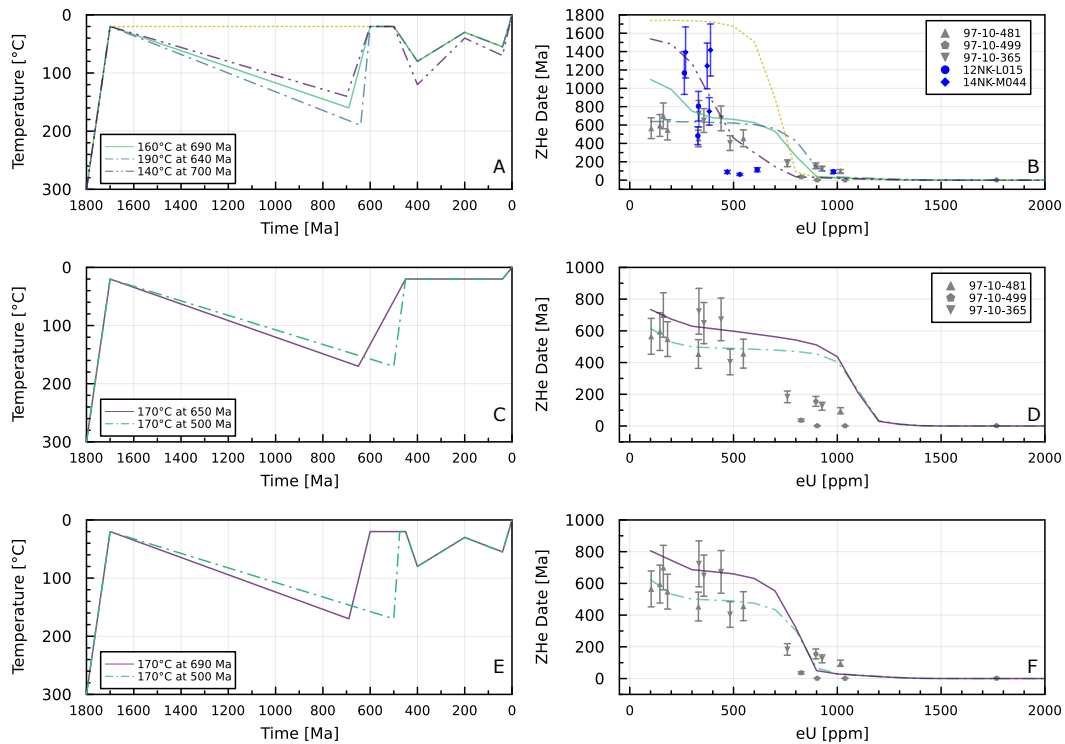


**Figure 4.** Forward thermal history modeling comparing different time-temperature scenarios (A, C, E) and resulting ZHe date-trends (B, D, F). Observed ZHe data are from Samples 1–2 and Sample 10 shown with 20% uncertainties. (A) Paths with maximum heating at 690 Ma (170 °C) and 640 Ma (190 °C) yield Neoproterozoic dates at low eU. Lower Neoproterozoic heating and greater magnitude/duration of heating in Phanerozoic produces older dates at low eU (140 °C at 700 Ma path). Initial cooling from metamorphic temperatures followed by no Proterozoic heating produces dates near 1700 Ma at low-to-moderate eU. Proterozoic heating is required to produce date-eU patterns consistent with the data. (B) Predicted date-eU patterns from  $t$ - $T$  paths in A. Note different y-axis scale. (C) Paths with maximum temperatures of 170 °C at 690 and 500 Ma, both without Phanerozoic heating. (D) Predicted date-eU patterns from  $t$ - $T$  paths in C; all dates near  $\sim$ 800–1000 ppm are overpredicted—demonstrating the need for Phanerozoic heating. (E) Paths with respective maximum temperatures of 170 °C at 690 and 500 Ma; cooling to surface temperature of 20 °C at 600 Ma and 475 Ma, followed by two thermal peaks at 400 Ma (80 °C) and 40 Ma (55 °C). (F) Predicted date-eU patterns from  $t$ - $T$  paths in E. Note that the time at surface temperature in the late Precambrian varies between models but does not significantly affect results due to minimal  $t$ - $T$  sensitivity at such conditions. See text for discussion.

age, are also preserved in the nearby Hudson Bay, Williston, and Michigan intracratonic basins (Allen & Armitage, 2011; Burgess, 2019).

A 690-Ma-cooling path yields an AFT age of ca. 520 Ma and an unprojected MTL of 12.0  $\mu\text{m}$ , within error of the measured MTL ( $r_{mr0} = 0.83$ ; Fig. 4E–F), whereas the AFT age for a 500-Ma-cooling path is much too young, ca. 410 Ma, yet produces a reasonable track-length distribution with a mean near 12.5  $\mu\text{m}$  due to rapid cooling. We can conclude from this that the AFT track lengths (unprojected MTL:  $12.35 \pm 1.2 \mu\text{m}$  and *c*-axis projected MTL:  $13.84 \pm 1.0 \mu\text{m}$ ) require relatively rapid cooling and that the timing of cooling tentatively precedes 500 Ma if there is any post-Cambrian heating—which is indirectly required by the combined ZHe, AFT and AHe data (Figs. 3 and 4C–D). Increasing the  $r_{mr0}$  to 0.80 predicts AFT ages of 550 Ma and an unprojected MTL of 12.55  $\mu\text{m}$  for the 690-Ma-cooling path, in better agreement with the measured data, whereas the 500-Ma-cooling path is nonetheless still too young, with the central age being ca. 425 Ma and MTL of 12.9  $\mu\text{m}$  (assuming Phanerozoic reheating). Post-Cambrian heating above  $\sim 80\text{--}85 \text{ }^\circ\text{C}$  will further reduce the AFT age ( $\ll 450 \text{ Ma}$ ) and begin to broaden the track-length distribution, with elevated temperatures making the length distribution bimodal at typical fluorapatite  $r_{mr0}$  values (0.83–0.84; refer to Fig. 3).

There are kinetic uncertainties for the AFT method to still consider, which stem from the challenges of extrapolating annealing kinetics over geological timescales and fully quantifying annealing variability related to apatite composition (e.g., Ketcham et al., 2007). Nonetheless, based on the forward modeling, the 500-Ma-cooling path does not well reproduce the real AFT data (i.e., real AFT age  $> 550 \text{ Ma}$ ). Collectively our observations reinforce an important point discussed in McDannell and Flowers (2020)—in deep-time applications, using multiple thermochronometers is critical to harness overlapping age and kinetic sensitivities, providing a more robust reconstruction of thermal histories while also mitigating potential biases inherent in single-thermochronometer datasets.

## 6.2 Geologic Context

The geologic history of the region provides key constraints for inverse thermal history modeling. In our models, geologic information is incorporated as discrete  $t$ – $T$  constraint ‘boxes’. These constraints ensure that randomly generated thermal histories within each



inversion are forced to pass through the box and are consistent with the known geological evolution of the region.

The widespread presence of the paleo-weathering surface beneath basal Paleoproterozoic sedimentary rocks, along with preserved paleosol horizons in some areas (Gall, 1992; Gall & Donaldson, 2006), provides reliable evidence for significant basement exposure during the Proterozoic. These geologic markers indicate that there was a period of exhumation before the formation of Proterozoic basins when basement rocks were exposed at the surface prior to depositional onset, which is directly informed by stratigraphic relationships and radiometric dating (Fig. 2). Basement rocks must have reached near-surface conditions, defined here as temperatures between 0–40 °C (equivalent to depths of ~0–1.5 km) by ca.  $1720 \pm 30$  Ma (Figs. 1 and 2).

During the latest Neoproterozoic to early Paleozoic, sea-level rise submerged most of Laurentia (e.g., Sloss, 1963, 1988; Allen & Armitage, 2011; Zhang, 2011), culminating in widespread inundation during the middle-late Cambrian (ca. 515–500 Ma) and in the middle-late Ordovician (ca. 460–450 Ma). This transgression is recorded in sedimentary rocks preserved in cratonic margin basins (Macdonald et al., 2023), the Foxe, Hudson Bay, and Williston intracratonic basins (Lavoie et al., 2019), and across the Canadian Arctic Islands (e.g., Ielpi and Rainbird, 2015; Fig. 1A). Isolated Paleozoic sedimentary outliers near the Paleoproterozoic basins (Fig. 1A) further document the widespread burial of the interior during this time (Bolton & Nowlan, 1979). Additional evidence for the timing of basement exposure (and subsequent burial) also comes from kimberlites in the Slave and Churchill cratons, including those in the Hornby Bay, Elu, and Bylot regions (Tappe et al., 2014; Mazrouei et al., 2019). Kimberlite pipes are commonly associated with emplacement at depths of < 2 km, as evidenced by the preservation of shallow pipe facies (i.e., crater, diatreme, and root) (Field & Scott Smith, 1999). Isolated Ediacaran-Cambrian and younger Mesozoic kimberlites across northern Canada contain sedimentary xenoliths, indicating that some areas of the Churchill-Slave cratons were buried beneath sedimentary cover during the Proterozoic (Masun et al., 2004), Paleozoic (Cookenboo et al., 1998), and Mesozoic (Webb et al., 2008).

A key point about the near-surface geologic constraints is that while the ages of sedimentary rocks are known, uncertainty remains about when the basement was initially re-exhumed, since sedimentary strata only provide a minimum exposure age. For example,

there is a lengthy hiatus between ca. 720–515 Ma in the Canadian Arctic Islands (Macdonald et al., 2023; Fig. 1A)—indicating that in some shield locations, crystalline basement was possibly exposed for up to 200 Myr before Cambrian transgression. The timing of basement exposure preceding Paleozoic burial remains uncertain but likely occurred prior to the Cambrian. Notably, we cannot ‘test’ the precise timing of basement exposure (in the form of a model surface constraint) due to the insensitivity of most thermochronometers to such low temperatures (e.g., Green & Duddy, 2021). To illustrate this, the inversion presented for Samples 1–2 was modeled without an Ediacaran-Paleozoic surface constraint in McDannell and Keller (2022) (also see Fig. 5 below). Near-surface temperatures of  $> 0\text{--}50\text{ }^{\circ}\text{C}$  are permitted by the data between ca. 620–450 Ma. These data were remodeled here with enforced geological constraints to ensure consistency with our other samples, but the resolved thermal history did not change appreciably.

We account for uncertainty in the timing of basement exposure in our  $t\text{--}T$  boxes, reflecting [i] minor variations in Proterozoic basin depositional onset (Fig. 2), [ii], the regional late Neoproterozoic hiatus, and [iii] subtle age differences in local Paleozoic strata (i.e., McDannell and Keller, 2022; Figs. 1 and 2). We placed a conservative constraint within the later part of the 720–450 Ma hiatus interval between 600–450 Ma ( $0\text{--}40\text{ }^{\circ}\text{C}$  allowed) that requires a single  $t\text{--}T$  point within that region of the model general prior. It is important to clarify that QTQt does not prevent paths from cooling *earlier* to the near-surface relative to the  $525 \pm 75$  Ma constraint box, since QTQt tests non-monotonic path trajectories regardless of constraint box arrangement. Due to Bayesian prior assumptions, however, the relative probability of such  $t\text{--}T$  paths is often lower since the additional path complexity cannot be directly informed by the data.

### 6.3 Inverse Modeling

Forward modeling exercises, along with geologic information, provided useful context for inverse modeling. The QTQt software v. 5.8.0 (Gallagher, 2012), which implements a reversible jump Markov chain Monte Carlo algorithm to adaptively search for suitable  $t\text{--}T$  paths, was used to invert our multi-method thermochronological datasets (refer to the SI for model output). QTQt modeling methods are similar to those discussed in McDannell, Keller, et al. (2022b) and McDannell and Keller (2022). The new and previously published ZHe and AHe data were modeled with uncorrected dates calculated internally by QTQt using the measured U, Th, Sm, and He. Model results were evaluated based on acceptance

rates of time and temperature jumps being within the normal bounds of approximately 0.1–0.6, and more importantly, established stationarity of the Markov chain, which often requires sampling of at least 500,000 to 1,000,000 iterations during burn-in for deep-time applications with multiple thermochronometers (McDannell, Keller, et al., 2022b; McDannell & Keller, 2022).

The ZHe date uncertainties were evaluated by applying 10–30% Hierarchical Bayes (Malinverno & Briggs, 2004) resampling in QTQt (i.e., 1–3× the input 10% ZHe uncertainty). This is much less than the QTQt default 1–100× used in McDannell, Keller, et al. (2022b) and is considered a very conservative strategy to estimate the total date error that may still lead to relative statistical misfit between model dates and observed dates. The source of this misfit is related to underestimated total errors, both kinetic and geological, that vary in relative magnitude for different zircon grains within a date-eU trend. Radiation-damage kinetic model calibration (e.g., misfit at either low or high He diffusivity) or uncharacterized U-Th zonation are the most likely sources (Anderson et al., 2017; Guenthner, 2021). For example, older low-eU zircon dates may have larger total analytical errors compared to younger, potentially metamict (high-eU) zircons, whereas the latter have smaller relative uncertainty but are less constrained by diffusion kinetic experiments. This behavior is especially true for high-eU zircons where model age prediction differences of up to 50–100 Myr are possible for deep-time histories (e.g., Guenthner, 2021).

Apatite He date uncertainties were fixed at 10% and were not resampled. The  $r_{mr0}$  parameter was instead resampled within QTQt and allowed to vary to account for possible kinetic effects of apatite composition on damage annealing susceptibility (McDannell & Issler, 2021). Resampling date uncertainties and the  $r_{mr0}$  kinetic parameter indirectly account for unquantified sources of geological age dispersion and kinetic model uncertainty. Importantly, all the *measured* analytical dates are jointly inverted for the inversions discussed herein.

We first examine a QTQt inversion of Samples 1–2 that includes additional ZHe data from nearby Sample 10, yielding similar results (to the other discussed models) without an imposed Ediacaran-Paleozoic surface constraint (Fig. 5). This inversion includes one of the largest combined datasets reported in our paper and independently supports constraint box placement in the other inversions (see below) because the combined ZHe, AFT, and AHe data can indirectly constrain the time at low temperatures in the latest Precambrian. The

QTQt inversion shows the full distribution of accepted  $t$ - $T$  paths alongside representative paths (Fig. 5)—we introduce these specific  $t$ - $T$  paths from the posterior only for the purpose of discussing model behavior. For all other inversions presented in this paper, we opted to show the full marginal posterior  $t$ - $T$  distribution rather than place undue significance on any one  $t$ - $T$  path.

The Maximum Likelihood (ML) path, shown as a red curve, is the best-fitting model and typically contains the greatest number of  $t$ - $T$  points or highest complexity. The Maximum Posterior (MP) path, shown in green, corresponds to the thermal history with the highest posterior probability and is generally the simplest model with the fewest  $t$ - $T$  points. Within QTQt, the posterior probability is calculated by combining the likelihoods and prior probabilities for each model path, balancing data fit with model complexity. The Maximum Mode (MM) solution, depicted as a gray curve, is constructed at 1-Myr intervals by following the peak of the marginal distribution. Meanwhile, the Expected model (EX), shown by black curves with the 95% credible interval, is the approximate weighted average of the marginal distribution. It is important to note that the MM and EX models are not exact solutions but summaries of the accepted history pool (Gallagher, 2012, for discussion).

Bayesian inversion emphasizes parsimony by favoring simpler models unless the data strongly support more complex histories. For example, the Maximum Posterior and Maximum Likelihood models differ overall in complexity and style, but are very similar where the model has the highest  $t$ - $T$  resolution during Neoproterozoic cooling (Fig. 5). Following the requirement of surface exposure during the late Paleoproterozoic (16 °C at 1655 Ma), the key  $t$ - $T$  points along the simpler Maximum Posterior path are 175 °C at 726 Ma and 4 °C at 618 Ma, whereas that same interval for the Maximum Likelihood path is more complex, with points at: 188 °C at 714 Ma; 184 °C at 712 Ma; 45 °C at 657 Ma; 60 °C at 579 Ma; and 7 °C at 495 Ma. The additional complexity is common with the ML path, as small iterative  $t$ - $T$  node variations may result in minimal or no improvement in the [log] likelihood, yet such models can still be accepted. Although both of these  $t$ - $T$  paths are relatively simple, every point along them aligns remarkably well, or does not conflict with, independent geological evidence, including, regional Precambrian and Jurassic basement exposure as well as Ordovician-Devonian and Cretaceous-to-Miocene burial events represented in the younger Phanerozoic intracratonic basins (e.g., Osadetz et al., 2002; Galloway et al., 2012; Lavoie et al., 2019; McDannell & Keller, 2022). In this sense, geologic data can serve as hold-out information for validating models (e.g., Kuhn & Johnson, 2013).

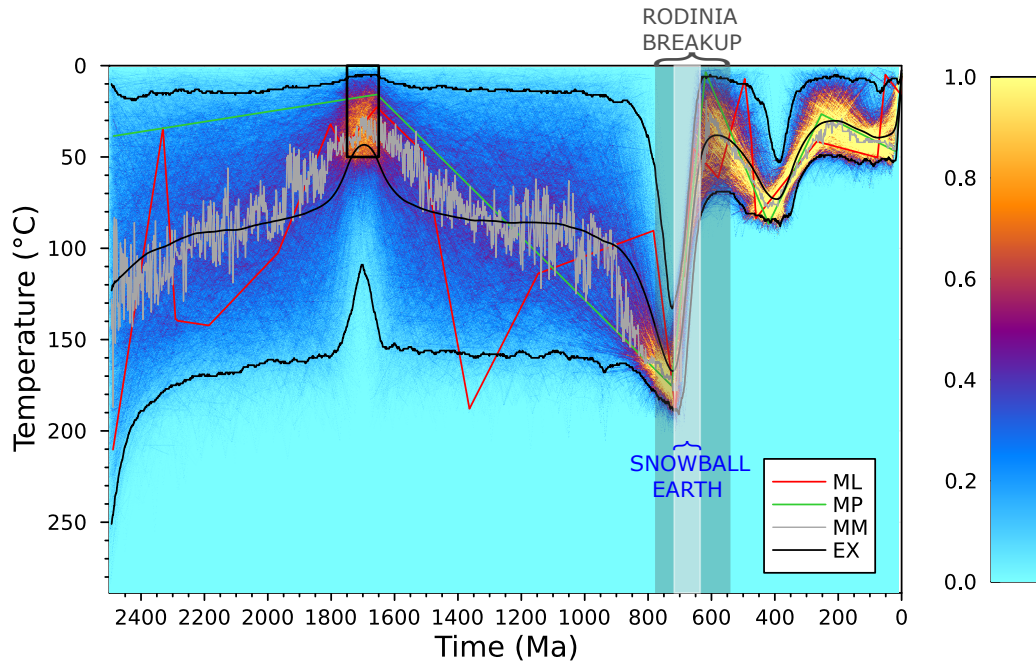


**Figure 5.** QTQt inversion of samples 97-10-481, 97-10-499, and 97-10-365 that include ZHe, AFT, and AHe data (first two samples published in McDannell and Keller, 2022). Marginal posterior thermal histories shown as a heat map of path density resolved to a pixel size of 1 Myr and 1 °C. Relative probability is proportional to path density, where brighter colors and higher saturation indicate more accepted thermal histories pass through that region of  $t$ - $T$  space. Color scale is the normalized path density (minimum value of 0 is equal to no paths, and a maximum value of 1 is equal to the upper 95th percentile of path density). General model prior: 0–2500 Ma and 0–300 °C. Maximum allowed heating-cooling rate of 3 °C/Myr with modern surface temperature 0–5 °C. Only the Paleoproterozoic geologic surface constraint is enforced in the model between 0–50 °C (see discussion and Fig. 6 below). ML = Maximum Likelihood model path; MP = Maximum Posterior model; MM = Maximum Mode model; EX = Expected model. The MP model is typically the ‘preferred’ model in a Bayesian context. Important MP path  $t$ - $T$  points are: 175 °C at 726 Ma and 4 °C at 618 Ma; 86 °C at 420 Ma; 27 °C at 253 Ma; 47 °C at 20 Ma; and 5 °C at 0 Ma. White bar denotes the Sturtian (717 Ma to 659 Ma) and Marinoan ( $646 \pm 5$  Ma to 635 Ma) glaciations and gray bar is timing of supercontinent Rodinia breakup. Note that model cooling is synchronous with both snowball glaciations.

## 6.4 Interpretation of Time-Temperature Inversions

Building on the previously discussed single QTQt example, the thermal histories of shield samples reveal notable similarities, primarily documenting the  $< 200$  °C  $t$ - $T$  history of Churchill Province rocks (Fig. 6). Heating and cooling events in these  $t$ - $T$  models are interpreted as being linked to episodes of sedimentary burial and subsequent erosion. Samples from the now-exposed crystalline basement require heating and thermal resetting after near-surface exposure at ca. 1700 Ma (Figs. 3 and 4). The models incorporating integrated mineral systems were partially reset, while those with only low-temperature chronometers (e.g., models 5, 6, 9) provide limited information following required Meso- to Neoproterozoic resetting. Inversions 1–2, 3, 4, 7, and 8 include ZHe and AFT dates that constrain Mesoproterozoic burial heating (Fig. 6). Some of our inversions lack adequate resolution to resolve thermal history detail in the Mesoproterozoic (e.g., models 5, 6, and 9) but still require elevated temperatures ( $> 120$  °C) and deep sedimentary burial in the Neoproterozoic. In all models, the coupled ZHe and AFT data primarily constrain the timing of cooling from temperatures around 150–110 °C during the Neoproterozoic, with most cooling occurring between ca. 690–630 Ma (Fig. 6). Despite finite  $t$ - $T$  sensitivity, all models consistently constrain Neoproterozoic cooling. The episodic heating and cooling pattern in the Phanerozoic (Fig. 6, models 1–2, 5, 6, 9) aligns with the well-documented ‘two-peak’ thermal histories across the Canadian Shield.

## 7 Discussion

### 7.1 Implications for Proterozoic Basin Evolution

The timing and magnitude of heating in  $t$ - $T$  inversions from samples among basins broadly agree and demonstrate that the exposed basement was also buried under Proterozoic sedimentary cover (Fig. 6). Our  $t$ - $T$  models refute the assumption that the basement surface was subaerially exposed, or nearly so, for most of the Proterozoic (Figs. 4, 5, and 6) and provide the first evidence that the Athabasca, Thelon, Hornby Bay, and Elu basins may have been connected across a broader region of interior Laurentia, similar to proposals for some North American Paleozoic basins (Sanford, 1987; Sloss, 1988; Lavoie et al., 2019; McDannell & Keller, 2022; McDannell, Pinet, & Issler, 2022). The basin area considered here is up to  $2 \times 10^6$  km<sup>2</sup> (Fig. 1B), similar to the preserved Neoproterozoic Centralian Superbasin in

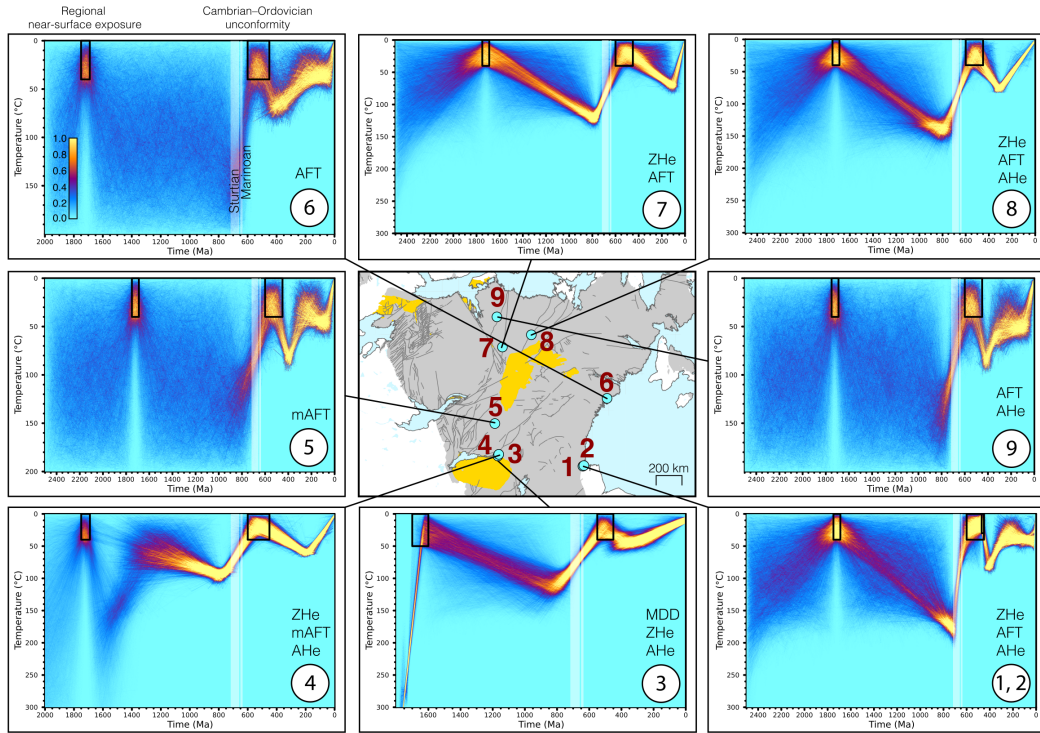


**Figure 6.** Thermochronological inversions for the central Canadian Shield. Inversions consisted of  $\geq 1,000,000$  burn-in iterations (discarded) and  $\geq 500,000$  iterations retained post-burn-in. The maximum allowed heating/cooling rate was specified as  $5 \text{ }^\circ\text{C Myr}^{-1}$  with a present day surface temperature of  $0\text{--}5 \text{ }^\circ\text{C}$ . Predicted model fits to the observed data are in the SI Figures S4–S10. The  $t$ - $T$  boxes assume near-surface conditions at ca. 1700 Ma and Ediacaran–Ordovician time (see text for discussion). All other model information is the same as Figure 5. White bars are the Sturtian and Marinoan glaciations.

Australia (Walter et al., 1995), or possibly comparable to the larger ( $\sim 3.5 \times 10^6$  km<sup>2</sup>) West Siberian Basin (Allen & Armitage, 2011).

The thermal histories for the Athabasca samples are particularly interesting since they are close to the center of the stable craton and have a well characterized geologic history (Fig. 6; Models 3–4). It is notable that Model 3 includes higher temperature potassium feldspar  $^{40}\text{Ar}/^{39}\text{Ar}$  information ( $\sim 350\text{--}200$  °C) that constrains initial exhumation from the deep crust (McDannell, Zeitler, & Schneider, 2018) and a subsequent history that is remarkably similar to Model 4. The geologic interpretation of the Athabasca region is that rapid post-orogenic cooling and exhumation to the surface occurred by ca. 1700–1675 Ma (Rainbird et al., 2007; Flowers et al., 2008; McDannell, Zeitler, & Schneider, 2018). Exhumation was followed by maximum burial heating in the Mesoproterozoic to  $\geq 120$  °C, or up to 150–200 °C (Flowers, 2009; McDannell, Keller, et al., 2022b). The total interpreted burial in this location equates to  $\sim 2.5\text{--}4.5$  km from  $< 1700$  Ma to ca. 700 Ma (see below). The central Athabasca Basin (e.g., Carswell impact structure) locally preserves up to  $\sim 2.3$  km of sedimentary strata (Athabasca Group; mainly sandstone) but in most areas does not exceed 1.5 km (Ramaekers et al., 2007). An elevated geothermal gradient of 40–45 °C km<sup>-1</sup> (Chu & Chi, 2016; Chi et al., 2018) and a conservative 100 °C of burial heating would imply a minimum 2.0–2.5 km of erosion in the Neoproterozoic. We propose that the Athabasca Basin was initially a minimum of  $\sim 3.7$  km thick, a similar estimate as Ramaekers et al. (2007), and locally up to 4.5 km thick—reconciling the long debated shallow ( $\sim 3$  km) versus deep ( $> 5$  km) burial models discussed by Chi et al. (2018).

The combined multichronometer dataset (Model 4) from Athabasca Basin potentially indicates two discrete episodes of burial and exhumation, however, the first heating event is relatively low probability in the model and is ‘bypassed’ by some histories, making it more similar to the other inversions (Fig. 6). Two periods of increased sedimentation are feasible across northern Canada given the similar burial and paleo-weathering record between correlative stratigraphic successions (Gall, 1992; Gall & Donaldson, 2006; Hahn et al., 2013; Rainbird et al., 2020; Pehrsson et al., 2023). The spatial continuity of this  $t\text{--}T$  signal is unclear and the events that occurred during the period between  $< 1500$  Ma to 1270 Ma are also less certain owing to differences in the preserved basin stratigraphy (Figs. 1 and 2).



The preserved regional geology nonetheless permits an interpretation of long-term burial (Fig. 2). For example, feeder dykes of the 1270 Ma Coppermine River Group flood basalt and Mackenzie diabase swarm cut the Athabasca, Thelon, and Hornby Bay basins (Rainbird et al., 2020), indicating that the shield experienced deposition from ca. 1700 Ma until 1270 Ma or later. Rainbird et al. (2020) strengthened the notion of regionally synchronous shallow-water carbonate sedimentation across the northern craton by determining a minimum depositional age of  $1438 \pm 8$  Ma (Figs. 1C and 2) for the lower Dismal Lakes Group of the Hornby Bay Basin (note that rocks overlie those dated). The distal Hornby Bay and Elu basins are capped by basalts of the ca. 1270 Ma Mackenzie LIP (Copper Creek and Ekalulia formations, respectively; Fig. 2), whereas the highly localized ca. 1540 Ma Look-out Point and Carswell Formation carbonates are the youngest preserved rocks in the more interior Thelon and Athabasca basins (Rainbird et al., 2020). At face value, these relationships imply that the more centrally located basins may have been more heavily eroded than those on the craton periphery based on stratigraphy alone, which is a reasonable inference considering the necessary long-term tectonic control on basin accommodation space.

The intervals between approximately 1700–1550 Ma and 1100–950 Ma are hypothesized as periods of widespread fluvial sheet sandstone deposition across Laurentia (Young, 1979; Rainbird et al., 1992). During these times, immense sedimentary basins likely developed on the craton in association with the supercontinents Columbia/Nuna (1.7–1.2 Ga) and Rodinia (1.1–0.7 Ga) (C. Wang et al., 2021). While the full spatial extent of basin deposition remains uncertain, our deep-time thermal history models provide valuable insights. The combined stratigraphy of the Hornby Bay and Amundsen basins (Fig. 1C) spans over 1670 Ma to 720 Ma. Notably, our thermal history models broadly align with this stratigraphy, suggesting extensive and near-continuous burial of the craton during this interval (e.g., models 7–8 with older ZHe dates; Fig. 6). However, an episodic burial history cannot be entirely ruled out (model 4, Fig. 6). Notably, there is no evidence for any of the remnant sub-basins rising again (i.e., regression) until after eruption of the 1267 Ma Coppermine River flood basalt,  $\sim 350$ –400 Myr after burial initiation.

The depth and extent of potential erosion and unconformity formation during the Mesoproterozoic are uncertain (Fig. 1C). Although it is unclear whether the older superbasin experienced significant erosion during this period, it is plausible that larger interior basins, such as Thelon and Athabasca, remained largely intact until the Neoproterozoic. By this time, the northernmost Laurentian craton was undergoing active subsidence (Young, 1979;

Rainbird et al., 2017; Greenman et al., 2021; Rainbird & Davis, 2022; Macdonald et al., 2023), and sedimentary deposits in continental margin basins (e.g., Amundsen and Bylot) reflect a phase of deposition that continued during and after the Grenvillian orogeny (Rainbird et al., 2017, 2020; Greenman et al., 2021). Our thermal history models and interpretive framework reinforce established models of transcontinental sedimentation pathways in the early Neoproterozoic from published studies of detrital zircon provenance (e.g., Rainbird et al., 1992).

Prior to the deposition of Grenvillian sediments in the younger distal basins (e.g., Amundsen Basin; Fig. 1), regional weathering and unconformity development occurred between  $< 1270$  Ma and 1100 Ma (Rainbird et al., 2020). A second burial phase followed, and lasted from  $< 1100$  Ma to 720 Ma (Fig. 1C), sufficient to thermally reset all low-temperature thermochronometers. Subsequent cooling and erosional exhumation are recorded by all thermochronometers analyzed in this study. Strata dating to ca. 1100–950 Ma and younger Neoproterozoic deposits are absent from interior Laurentia and are preserved only along the northern and western margins of the craton (Rainbird et al., 1992; Macdonald et al., 2023). Nevertheless, our thermal history inversions indicate that heating persisted into the late Neoproterozoic, until approximately 800–700 Ma. This timing coincides with the breakout of Laurentia from supercontinent Rodinia and the initiation of Sturtian glaciation.

We offer some explanations for our  $t$ - $T$  models exhibiting reheating into the Neoproterozoic (Fig. 6). First, it is possible that Mesoproterozoic through early Neoproterozoic sediments were deposited much more broadly across Laurentia—for example during the Grenvillian sedimentation episode (Rainbird et al., 2012)—but were stripped off at ca. 700–650 Ma, yet remained intact within the protected near-marginal areas of the craton with greater accommodation space made possible by “intracontinental” sagging and extension prior to Rodinian rifting (e.g., Rainbird et al., 1996, 2003). The superbasin may have been accommodation-limited and continued to subside in the Neoproterozoic around 1000–700 Ma. The Hornby Bay, Elu, Amundsen, and Bylot cratonic basins preserve Neoproterozoic sedimentary rocks (Fig. 1A) implying that if such sediments were deposited across the interior they were of modest thickness, which is reinforced by relatively thin carbonate and subordinate evaporite deposition during that interval (Fig. 1C). Additionally, early Neoproterozoic sediment supply may have waned or routing changed. Indeed, when basin accommodation is exceeded, cratonic depocenters switch from sediment sinks to sediment sources, or can be bypassed entirely by additional detritus when storage capacity is reached.

Lastly, Franklin LIP basalt outpourings may have caused additional kilometer-scale burial at ca. 720–718 Ma (Pu et al., 2022), which coincides with the approximate Neoproterozoic thermal maximum for most of our  $t$ - $T$  models (refer to discussion in Section 7.3 below).

## 7.2 Continental Denudation in the Neoproterozoic

In order to better understand the erosional patterns in the Neoproterozoic, we estimate the magnitude of exhumation. Cooling occurs in our models during the late Neoproterozoic and requires re-exhumation of the basement to the near-surface by ca. 600 Ma or earlier, or 450 Ma at the latest, based on local geology. Interpreted  $t$ - $T$  inversions generally place the currently exposed Precambrian basement of the Laurentian interior at temperatures of  $\sim$ 110–200 °C during the Neoproterozoic, corresponding to depths of  $\sim$ 2.4–7.6 km, assuming a surface temperature of 10 °C and a paleogeothermal gradient between 25 to 45 °C km<sup>-1</sup> for intracratonic basins (Kolawole & Evenick, 2023). We estimated an average burial and exhumation depth by assuming uniform distributions for surface temperature (0–15 °C), geothermal gradient (25–45 °C km<sup>-1</sup>), and the maximum heating temperature range derived from our models. By performing 10,000 random draws from these distributions, we approximated a mean unroofing depth of  $4.3 \pm 1.1$  km across all  $t$ - $T$  models, with a more conservative value being  $3.2 \pm 0.6$  km based on a narrowed, well resolved temperature range of 110–120 °C. Our estimates are further evidence that continental-scale erosion in the Neoproterozoic contributed to the formation of the North American Great Unconformity surface (e.g., DeLucia et al., 2018; McDannell, Zeitler, & Schneider, 2018; Keller et al., 2019; McDannell, Keller, et al., 2022b; McDannell & Keller, 2022); a prominent geological boundary that represents a significant gap in the rock record spanning hundreds of millions of years, where older Precambrian crystalline basement rocks are directly overlain by younger Paleozoic sedimentary rocks.

## 7.3 Supercontinent Breakup

Intracratonic basin formation is thought to result from lithospheric cooling, extension, and large-scale mantle downwelling during supercontinent assembly, while uplift and erosion are associated with mantle upwellings during supercontinent breakup (e.g., Allen & Armitage, 2011). The magnitude of Neoproterozoic cooling in our  $t$ - $T$  models (Figs. 5 and 6) highlights a period of extensive landscape evolution possibly driven by linked tectonic and surface processes. Weathering and erosion during the Neoproterozoic are evidenced

by the deposition of thick continent-derived clastic sedimentary rocks along the Laurentian margins (Macdonald et al., 2023, for summary). This period of erosion likely removed Neoproterozoic rocks and possibly much of the Paleoproterozoic-Mesoproterozoic basin strata that once covered the craton. Denudation onset occurred after ca. 800 Ma during the punctuated breakup of supercontinent Rodinia from ca. 780 Ma to 540 Ma.

Various tectonic processes emerge as plausible drivers of Neoproterozoic erosion during supercontinent breakup. The Franklin LIP, thought to have initiated Snowball Earth glaciations, notably coincides with the timing of widespread exhumation interpreted across Laurentia. A mantle plume led to the emplacement of the Franklin igneous province (Heaman et al., 1992), which is exposed on Victoria Island, just north of our sampled study area (Minto Inlier; Fig. 1A and C, Fig. 2). The thinning of the Shaler Supergroup beneath the Natkusiak Formation basalts (Fig. 1) has been interpreted as evidence of crustal doming preceding the onset of LIP volcanism (Rainbird, 1993). Continental extension and plume activity elevate mantle temperatures and generate large melt volumes—with much of the melt intruding and underplating the lower crust (Thybo & Artemieva, 2013), therefore, surface uplift and denudation are possible in the area affected by the plume (e.g., Rainbird & Ernst, 2001; McDannell, Zeitler, & Schneider, 2018).

Basalt eruptions began around 719 Ma during extroversion of Rodinia, just prior to the Sturtian Snowball Earth glaciation at 717 Ma (Pu et al., 2022). Pu et al. (2022) proposed that a volcanic plateau, possibly up to 2 km (?) thick, erupted and was then eroded across northern Laurentia. While the original Franklin basalt province may have spanned at least 2.5M km<sup>2</sup> across the Arctic (Macdonald & Swanson-Hysell, 2023), only feeder dykes remain preserved in the Churchill province, mapped north of 65° latitude. Some of our samples lie outside the inferred maximum southern LIP boundary, yet exhibit similar thermal histories to those samples within it, suggesting limited direct thermal impact on now-exposed basement rocks. In spite of these details, the temperature beneath a thick lava sequence increases mainly due to burial (e.g., Brown et al., 1994), which would still require at least 2 km of Neoproterozoic erosion after 719 Ma, which is consistent with the approximate initiation of cooling in our models.

Continental breakup may also trigger convective instabilities in the mantle that cause diachronous, widespread uplift and denudation. Gernon et al. (2024) proposed that cratonic margin extension causes lithospheric keel removal that propagates across a continent. The

Churchill cratonic lithosphere is poorly studied but is  $\sim 200$  km thick, and limited data suggest a depleted mantle signature typical of cratons (Tappe et al., 2014; J. Liu et al., 2016). However, a transition from lithospheric thinning, which facilitated Franklin LIP volcanism, to subsequent thickening would be required to restabilize the cratonic keel observed today (S. N. Stephenson et al., 2023). Thus, evidence for lithospheric thinning may be obscured by later mantle refertilization events that mended the cratonic root (J. Liu et al., 2021). Although not a perfect analogue, models of a propagating erosional front in South Africa indicate that such processes may require  $\sim 40$ – $50$  Myr to reach more than 1000 km inland from the rift margin, resulting in delayed erosion totaling  $\sim 1$ – $2$  km (Gernon et al., 2024). Given that our samples are located 1000–2000 km (or more) from any confirmed rift, and thermal histories suggest deeper exhumation, this mechanism appears insufficient to fully account for our observations but may potentially explain the last kilometer of unroofing just prior to the Cambrian.

The convective instability model also predicts that lithospheric delamination causes kimberlite magmatism. Latest Neoproterozoic-Cambrian kimberlites are preserved along the Slave craton margin to the west (ca. 613 Ma Coronation Gulf kimberlites), and in the eastern Rae craton, including the ca. 560 Ma Aviat cluster, ca. 540 Ma Pelly Bay field, and newly discovered ca. 556 Ma Mel kimberlites on Melville Peninsula (Kepezhinskas et al., 2024). Further to the northeast (nearly 1100 km from Sample 9), the oldest known examples are from the ca. 673 Ma Amon kimberlite-sill complex on northern Baffin Island (Tappe et al., 2014). Generally, kimberlite eruptions indicate heightened mantle perturbation and possible lithospheric modification during the latest stages of Rodinia breakup and are confined to the interval  $< 560$ – $530$  Ma. The spatial distribution of kimberlites indicates that volcanic systems exploited zones of thinner or weakened lithosphere (e.g., Tappe et al., 2014; Y. Wang et al., 2023) and are primarily located in the eastern Churchill-Rae domain, closer to the failed Ediacaran-Cambrian rift in the northern Arctic Islands (Macdonald et al., 2023). Most of the observed cooling in our  $t$ - $T$  models was complete or in final stages before many of the eruptions after 560 Ma. The scarcity of Tonian-Cryogenian kimberlites within the interior Churchill craton may reflect either a genuinely low eruption frequency during this period or preservation bias caused by truncation of the record by Snowball Earth ice sheets (Mazrouei et al., 2019).

#### 7.4 Snowball Earth Glaciations

A complementary explanation for Neoproterozoic unroofing is that wet-based ice sheets eroded Laurentia during the Cryogenian (Keller et al., 2019; McDannell, Keller, et al., 2022b; McDannell & Keller, 2022). The erosive potential of ice sheets during Snowball Earth events has been debated, with considerable focus on ice dynamics (e.g., cold-based versus wet-based conditions) and the intensity of the hydrologic cycle (Godd ris et al., 2011; Hoffman et al., 2017). Climate and ice-sheet models indicate that a significant portion of the simulated continental ice sheet is wet-based during a snowball, particularly for equatorial continents where basal sliding is anticipated (Donnadieu et al., 2003). Basal sliding may be maintained by geothermal heating under thick ice during prolonged multi-million year glaciations (Ojha et al., 2022).

Many Neoproterozoic successions display spatial and temporal variability, with sedimentary patterns and facies reflecting active ice dynamics, including dropstone rainout intervals and thick, glacially derived diamictite deposits (e.g., Condon et al., 2002; Allen & Etienne, 2008; Le Heron et al., 2013). Sedimentary geochemistry and climate modeling also suggest that as atmospheric CO<sub>2</sub> levels rise during Snowball Earth, the climate becomes increasingly sensitive to orbital forcing (Rieu et al., 2007; Benn et al., 2015; Mitchell et al., 2021). Consequently, ice sheet advance and retreat cycles, along with glacier-fed hydrological systems, were likely active during the later stages of a snowball period, leading to enhanced erosion and increased sediment transport.

Our inversions indicate a marked erosional interval of over 100–150 Myr across the Neoproterozoic (Fig. 6). Cooling in all our models initiates around 750 to 720 Ma and concludes by  $\geq 600$  Ma, with as much as 50% (or more) of this cooling necessarily occurring during the total  $\geq 64$  Myr of Cryogenian glaciation. Some examples with multiple thermochronometers and better  $t$ – $T$  resolution suggest that nearly all exhumation was within the Cryogenian (Fig. 5), with a peak near ca. 660 Ma (McDannell & Keller, 2022). Our best estimates of continental-scale upper crustal erosion align with both Snowball Earth events, coinciding with the Sturtian glaciation of Laurentia from 717 Ma to  $662 \pm 4$  Ma, and overlapping with the Marinoan glaciation between  $646 \pm 5$  Ma and 635 Ma (Rooney et al., 2015; Hoffman et al., 2017).

Thermal histories therefore suggest considerable exhumation firmly within the Cryogenian— with erosion during the waning stage of the Sturtian glaciation being one possibility. While

speculative, if physical weathering and erosion ensued during the end-Sturtian, chemical weathering of a large volume of fresh, comminuted sediments in the subsequent interglacial could stimulate silicate weathering (e.g., Mills et al., 2011) and help trigger the Marinoan snowball. This proposition holds promise in light of evidence that basaltic LIP terrains were consumed, to a large degree by erosion and weathering before and during the Sturtian period (Cox et al., 2016).

Exhumation does not necessarily require deep incision of crystalline basement rocks, but instead it may include sedimentary cover sequences, metasedimentary units, or volcanic deposits that were previously overlying the crystalline basement and are more susceptible to erosion. Proterozoic basin rocks would have been highly susceptible to erosion by ice sheets. For context, the Quaternary Eurasian ice sheet exhibited a mean erosion rate of  $\sim 0.8 \text{ mm yr}^{-1}$  in platform regions primarily covered by sedimentary rocks (Patton et al., 2022), which is similar to the compiled global long-term average rate of  $\sim 0.5 \text{ mm yr}^{-1}$  for different glacier types across  $\sim 10^{-2}$  to  $10^8 \text{ yr}$  timescales (Wilner et al., 2024). Achieving equivalent erosion rates would require only moderate basal ice sliding velocities of  $\sim 12\text{--}25 \text{ m yr}^{-1}$ , as estimated using an empirically derived glacial erosion law (Cook et al., 2020). Those values fall within the lower range of predicted rates ( $\sim 1\text{--}50 \text{ m yr}^{-1}$ ) for wet-based ice sheets in Snowball Earth climate simulations across the Laurentian interior (Donnadieu et al., 2003). Three to four kilometers of supracrustal rocks could be removed in  $\sim 3.8\text{--}5.0 \text{ Myr}$  at the quoted Eurasian ice sheet erosion rate, which is only  $\sim 7\text{--}9\%$  of the 58 Myr duration of Sturtian glaciation.

Although there is uncertainty beyond the more precise snowball chronologies, our results for the North American cratonic interior suggest cooling and deep exhumation ( $\sim 4 \text{ km}$ ) during Snowball Earth glaciations within a broader interval of Laurentian tectonic reorganization (Fig. 5). The Cryogenian may represent a unique time in Earth history when global glaciation and tectonic and eustatic processes related to the breakup of supercontinent Rodinia combined to drive unprecedented and extreme continental erosion, particularly in low-latitude continents with more dynamic ice sheets (Donnadieu et al., 2003). Positive dynamic topography would favor emergent landmasses and  $> 3$  to  $5 \text{ km}$ -thick ice sheets would produce relative sea level fall  $> 400 \text{ m}$  (Y. Liu & Peltier, 2013; Creveling & Mitrovica, 2014; Hoffman et al., 2017) and large potential energy gradients (gravitational/erosional) across continents. The impact of glaciation on cratonic shields is undeniable, particularly in regions with minimal topography and little to no evidence of significant tectonic modi-

fication over hundreds of millions of years. The subdued topography itself may represent the most visible legacy of prolonged and repeated continental ice sheet activity. This model offers a testable framework for future investigation, enabling specific predictions about the interactions between tectonic, climatic, and geochemical processes in the Neoproterozoic.

### **7.5 Neoproterozoic Glacial Erosion of Laurentia Recorded by Detrital Zircons**

Dynamic ice sheets may also help explain characteristics of glacial strata accumulated during Snowball Earth events. If a vast Proterozoic superbasin underwent extensive erosion in the Neoproterozoic, we would expect an abrupt influx of Archean-Proterozoic sediments (i.e., detrital zircon; DZ) in Cryogenian pericratonic rift-basin deposits. A pre- and syn-glacial stratigraphic record are required to test this proposal and we do so by closely examining both the western (Canada/Idaho, USA) and eastern (Scotland) margins of Laurentia in detail.

The glacial influence on continental erosion and sedimentation has long been a focus of research along the Laurentian margin (e.g., Aalto, 1971; Ross, 1991; McMechan, 2000; Smith et al., 2011). Multiple Neoproterozoic rift margin successions in North America preserve Cryogenian sedimentary strata, including Snowball Earth glacial diamictites and cap carbonates exposed in locations such as the Mackenzie-Ogilvie Mountains (Yukon, Canada), Death Valley (California, USA), and southeastern Idaho (USA) that directly support a Cryogenian icehouse (Macdonald et al., 2010; Hoffman et al., 2017; Isakson et al., 2022; Macdonald et al., 2023).

An intact sediment record of Neoproterozoic glaciation is globally rare and the lithostratigraphy along western Laurentia is complicated by syn-sedimentary tectonic deformation (Young, 1979; Ross, 1991). The distal western margin shelf edge is characterized by rift-faulted blocks with preserved glacio-volcanic infill and a commonly prominent sub-Cambrian unconformity surface, providing evidence of erosion across a broad area (i.e., the Great Unconformity). For example, the ca. 730–570 Ma Windermere Supergroup accumulated in fault-bounded rift depressions along the western margin of Laurentia and contains abundant evidence of glacially influenced sedimentation (Ross, 1991; Hadlari et al., 2021). The lower Windermere primarily consists of a coarse-grained submarine fan diamictite assemblage of feldspathic conglomerate and pebbly sandstone “grits” with interbedded grey-black



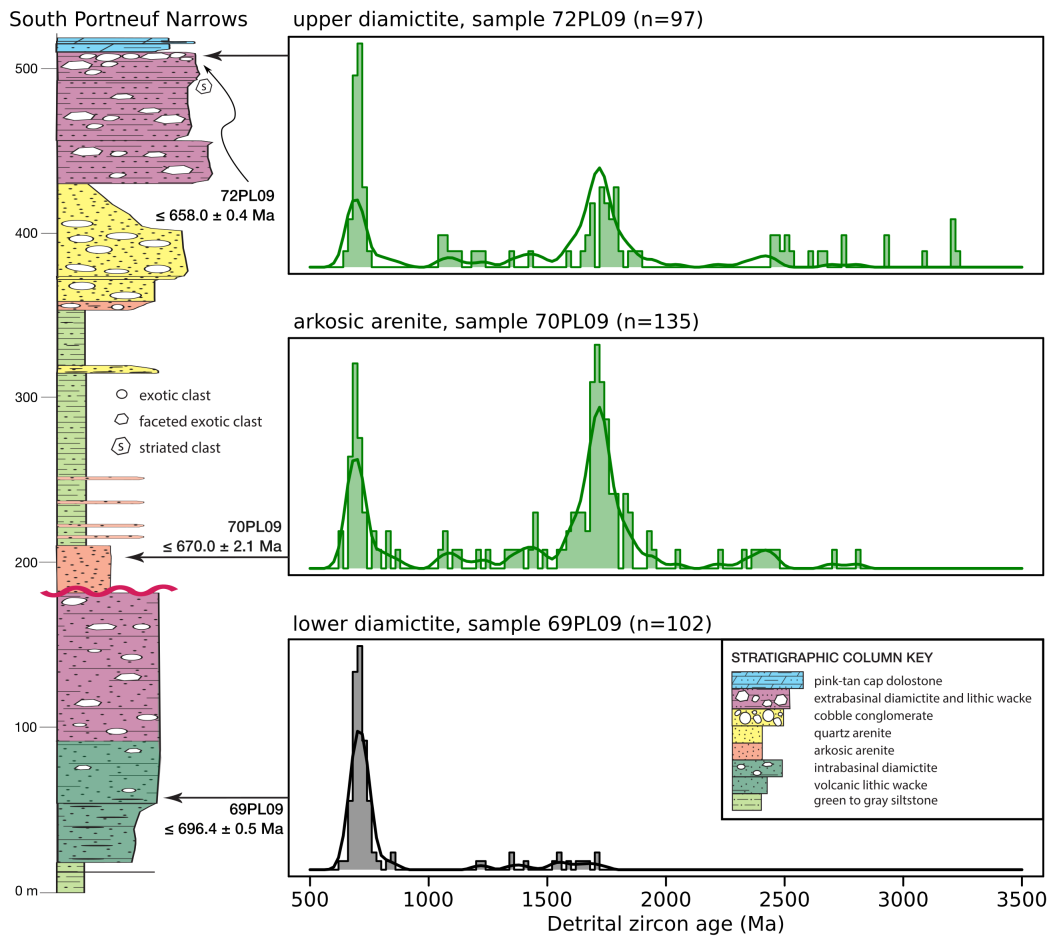


**Figure 7.** Detrital zircon U-Pb concordia age stratigraphy of the Pocatello Formation, Idaho. Stratigraphic column modified from Isakson et al. (2022). Single-grain concordia ages (Ludwig, 1998) were calculated in IsoplotR (Vermeesch, 2018) from the published  $^{207}\text{Pb}/^{235}\text{U}$ ,  $^{206}\text{Pb}/^{238}\text{U}$ , and  $^{207}\text{Pb}/^{206}\text{Pb}$  ratios (Isakson et al., 2022). Similarly, we retained only those grains with  $\geq 90\%$  concordance (i.e., the concordia distance from Vermeesch, 2018). Normalized kernel density estimation (AverageShiftedHistograms.jl) calculated over a fine-partition histogram of DZ ages (20 Myr bin) with a quartic biweight kernel smoothed over four adjacent histograms. CA-ID-TIMS U-Pb zircon dates (shown by arrows) are the maximum depositional ages of the sampled units from Isakson et al. (2022).

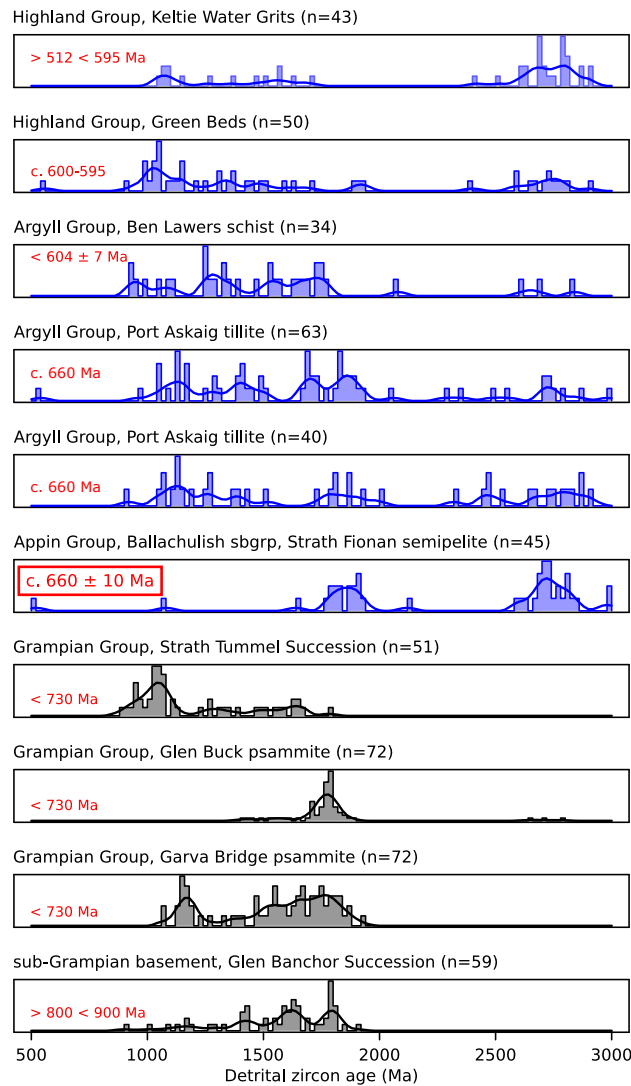


**Figure 8.** Detrital zircon U-Pb concordia age stratigraphy of the Dalradian Supergroup, from the central Highlands, Perthshire, Scotland. An abrupt appearance of Archean-Paleoproterozoic zircons occurs near 660 Ma during terminal Sturtian glaciation. Original data published by Cawood et al. (2003). Data shown here were recalculated and plotted using the same methods as the Pocatello Fm. dataset in Figure 7. The data presented here differ slightly from the original dataset in terms of date calculation and the number of grains shown, but this does not affect the ages or distributions in any meaningful way. Approximated depositional ages of the sampled units shown on left of each panel (red text) from Cawood et al. (2003, 2007) and Moles and Selby (2023). Note that the Port Askaig tillite is shown twice according to original sampling.

argillite interpreted as representing glaciomarine sedimentation (e.g., Toby Formation) and correlates regionally with glaciogenic diamictites (Aalto, 1971; Smith et al., 2011; Macdonald et al., 2023). Such interbedded conglomeratic gravel and clay-rich deposits have been linked to ice melt-water pulses during more recent Alpine glacial cycles (Florindo et al., 2024).

The Neoproterozoic stratigraphy of southeast Idaho (western USA) is well dated and characterized by pre-, syn- and post-glacial strata (Isakson et al., 2022), making it an ideal location to test our hypothesis. The Pocatello Formation is distinguished by mostly siliciclastic, minor volcanics, and rare carbonates, including glacial diamictites and cap dolostones representing both the Sturtian and Marinoan glaciations (Hoffman et al., 2017) (respective “lower” and “upper” diamictites of Isakson et al. 2022). Generally, these rocks have been interpreted as continent-derived immature to mature sedimentary rocks deposited in subaqueous environments that contain reworked glacial detritus, including striated and faceted clasts (Isakson et al. 2022; Fig. 7). The Pocatello Formation notably displays an up-section shift to older Paleoproterozoic and Archean detrital zircon age populations (Fig. 7), potentially signifying an increase in glacial incision between ca. 670–658 Ma, in agreement with nearby thermochronological estimates (McDannell & Keller, 2022). The detrital zircon U-Pb data compilation published by Isakson et al. (2022) demonstrates that the lower Sturtian diamictite in South Portneuf Narrows is characterized by 700 Ma volcanic age peak and minor ca. 1500 Ma grain population, whereas the  $\leq 670$  Ma arenite unconformably overlying the lower diamictite contains an additional and pronounced 1700–1900 Ma Hudsonian component, and minor  $> 2400$  Ma age population (Fig. 7). The top of the Marinoan upper diamictite contains more dominant and abundant 2500–3200 Ma zircon grains characteristic of an Archean crystalline basement or reworked sedimentary source. A comparable DZ signal was also documented in the Windermere Supergroup in the Canadian Cordillera by Hadlari et al. (2021) where an influx of recycled Grenvillian Sequence B zircon grains is present in the syn-rift Toby Formation, whereas Hudsonian and Archean U-Pb ages appear higher in the passive margin strata.

Similar to the sedimentary succession in Idaho, the detrital zircon stratigraphy of the Dalradian Supergroup in Scotland provides another window into the timing and pattern of sedimentation in the Neoproterozoic along eastern Laurentia. Cawood et al. (2003) discussed the detrital zircon relationships in the Dalradian and a primary conclusion of their work was that Dalradian rocks were sourced from Laurentia. In addition, they recognized that the

sub-Grampian basement and overlying Grampian Group contain mostly Paleoproterozoic–Mesoproterozoic zircons with rare Archean grains (Fig. 8). A dramatic appearance of Archean zircons then occurs in the overlying Appin, Argyll, and Southern Highland Groups of the upper Dalradian Supergroup (Fig. 8). To put this into perspective, Archean zircons only represent 1% of the total concordance-filtered sub-Appin Group population, whereas ~32–33% of the zircons in the overlying rocks are Archean. This DZ age trend consistently appears in other studies of Dalradian rocks across Scotland (e.g., Cawood et al., 2007; Strachan et al., 2013).

The importance of the Dalradian succession becomes more apparent when the approximate position and timing of the shift to older ages is examined in stratigraphic context (Fig. 8). The boundary between the Appin and Argyll groups is marked by the Port Askaig tillite, which has been assigned to both the Sturtian and Marinoan glaciations based on carbon and strontium stable isotope data (Moles & Selby, 2023, for discussion). The effects of Paleozoic metamorphic overprinting and a lack of time markers in the Dalradian have hindered an unambiguous interpretation of the chronostratigraphy for decades. A depositional age of  $659.6 \pm 9.6$  Ma was determined for the Ballachulish Slate Formation (Rooney et al., 2011)—positioned below the tillite within the same stratigraphic interval sampled by Cawood et al. (2003) for detrital zircon analysis. Recently, Moles and Selby (2023) applied Re-Os dating of pyrite to constrain the age of rocks in the [overlying] lower Argyll Group to  $604 \pm 7$  Ma and suggested the Port Askaig was Marinoan (Ben Lawers schist overlies dated unit; Fig. 8). The fragility of the Re-Os system in pyrite, however, prevents unambiguous interpretation of this date as a primary depositional age. The Port Askaig Formation being Sturtian in age is indirectly supported by similarities in carbon isotope chemostratigraphy with other better dated Sturtian strata (e.g., Prave et al., 2009; Fairchild et al., 2018). Therefore, the Appin and lower Argyll Groups together place the appearance of Archean detrital zircons in the tillite at ca. 660 Ma during the terminal Sturtian cryochron (Fig. 8).

The abrupt increase in Archean-Proterozoic zircons in the Sturtian indicates a plausible genetic link between the sediments bearing Archean zircons and ice sheet glaciation—which is anticipated if Laurentian cratonic basins, composed of mostly Archean-Paleoproterozoic detritus, were heavily eroded in the Cryogenian as suggested by our  $t$ - $T$  models. Indeed, the commonly held interpretation is that the Laurentian rocks from younger orogens, like the Grenville Mountains, were progressively uplifted and eroded followed by exposure and denudation of Archean basement rocks during continental rifting (Cawood et al., 2003).

Such a model is tenable, assuming the Archean zircons are first cycle—whereas a complementary explanation is one of sediment recycling, since the Proterozoic interior basins were an abundant ancient detrital zircon source.

The nature and timing of the shift to older, craton-derived zircons in the Dalradian Supergroup (Fig. 8) is similar to that observed in the Pocatello Formation (Fig. 7) and elsewhere along the western Laurentian margin (e.g., Hadlari et al., 2021). This consistent pattern suggests multiple areas received syn-glacial pulses of craton-derived zircon grains during the terminal Sturtian (and/or Marinoan) glaciation. In support of our thermal history models, the detrital zircon records from these Laurentian localities suggest that Cryogenian ice sheets eroded ancient zircon grains from Neoproterozoic sheet sandstones and the Paleoproterozoic interior basins ( $\pm$  metamorphic basement) that were subsequently transported to the continental periphery and deposited in Rodinian rift basins.

### 7.6 The Cratonic Sedimentary Record and ‘Missing Time’

Deep exhumation in the Neoproterozoic establishes limits on the pace and magnitude of erosion (given plausible sediment accumulation rates) that would produce a large erosional unconformity and still permit survival of the older, isolated Proterozoic cratonic basin deposits over nearly a billion years. The global sedimentary record compilation of Ronov et al. (1980) provides insight into the nature of exhumation in the context of cratonic basin preservation.

It is well established that depositional rates are limited by tectonic subsidence and accommodation space at long time scales (e.g., Allen & Allen, 2013). Sediment accumulation rates in cratonic basins are low—on the order of  $\sim 5\text{--}10$  m Myr<sup>-1</sup> (Schwab, 1976); increasing to  $\sim 20\text{--}30$  m Myr<sup>-1</sup> if hiatuses are excluded (Sloss, 1988; Allen & Armitage, 2011). Comparable accumulation rates are reported for North American cratonic basins in the Paleozoic and are even lower,  $3\text{--}4$  m Myr<sup>-1</sup>, for platform areas outside of basins, e.g., the Transcontinental Arch (Sloss, 1988). Husson and Peters (2017) determined that Precambrian sedimentation rates were comparable to those in the Phanerozoic—supporting uniformity across geologic time. Thus, if we first assume that continental sedimentation rates have remained nearly constant over long timescales (Schumer & Jerolmack, 2009), and that the global average volumetric sediment flux of  $1.18$  km<sup>3</sup> yr<sup>-1</sup> during the Phanerozoic

determined by Ronov et al. was similar during the Precambrian, we can then infer the missing strata removed (i.e., ‘missing time’) due to erosion in the late Neoproterozoic.

The vertical sediment accumulation rate derived from Ronov et al. equates to 7.93 m Myr<sup>-1</sup> across global continental area. A similar average Phanerozoic accumulation rate of 5.74 m Myr<sup>-1</sup> is derived from the Macrostrat database for North America (Peters et al., 2018). If a global average of  $\sim 4$  kilometers of upper crust was eroded in the Neoproterozoic (e.g., Keller et al., 2019), which agrees with a broader Laurentia-wide denudation signal from thermochronology (DeLucia et al., 2018; McDannell, Zeitler, & Schneider, 2018; McDannell, Keller, et al., 2022b; McDannell & Keller, 2022), then sedimentary rocks would be missing from the Precambrian stratigraphic record that represent ca. 500 Myr to 700 Myr of [accumulation] time using the respective Ronov and Macrostrat estimates (Fig. 9). Put simply, these calculations provide a first-order approximation of the age range of strata plausibly eroded in the Neoproterozoic based on the magnitude of the cooling signal from our thermal history models. The potentially eroded package of sedimentary rock would equate to sediment deposition between ca. 700–1200 Ma (assuming Ronov rates) or ca. 700–1400 Ma (assuming Macrostrat rates).

In this simple scenario, removal of Precambrian sedimentary rocks extending back to ca. 1400 Ma would be permitted by applying the more conservative Macrostrat sedimentation rate for North America. For comparison, the youngest dated sedimentary rocks within the intracratonic basins are the < 1440 Ma carbonates (Fig. 2). The observed stratigraphic gap thus appears to be consistent with that expected from  $\sim 4$  km of erosion and provides an explanation for why ca. 1000 Ma Grenvillian sandstones are not preserved in the continental interior. Interestingly, this also implies that locations hosting structurally preserved Proterozoic sedimentary rocks that survived basin fragmentation have undergone minimal further erosion since the Cryogenian. Removal of all Proterozoic sedimentary cover would require deeper erosion of  $> 5.5$  km (Fig. 9), or alternatively, lower assumed sedimentation rates of  $\sim 3$ – $4$  m Myr<sup>-1</sup>, which are feasible in accommodation-limited environments. Spatial patterns of exhumation and the preserved basin stratigraphy (Fig. 2) therefore align with our simple sediment flux model. Our  $t$ – $T$  models and other proxy data support long-standing hypotheses regarding the deposition and erosion of the missing upper sections of Proterozoic intracratonic basin stratigraphy in northern Laurentia.

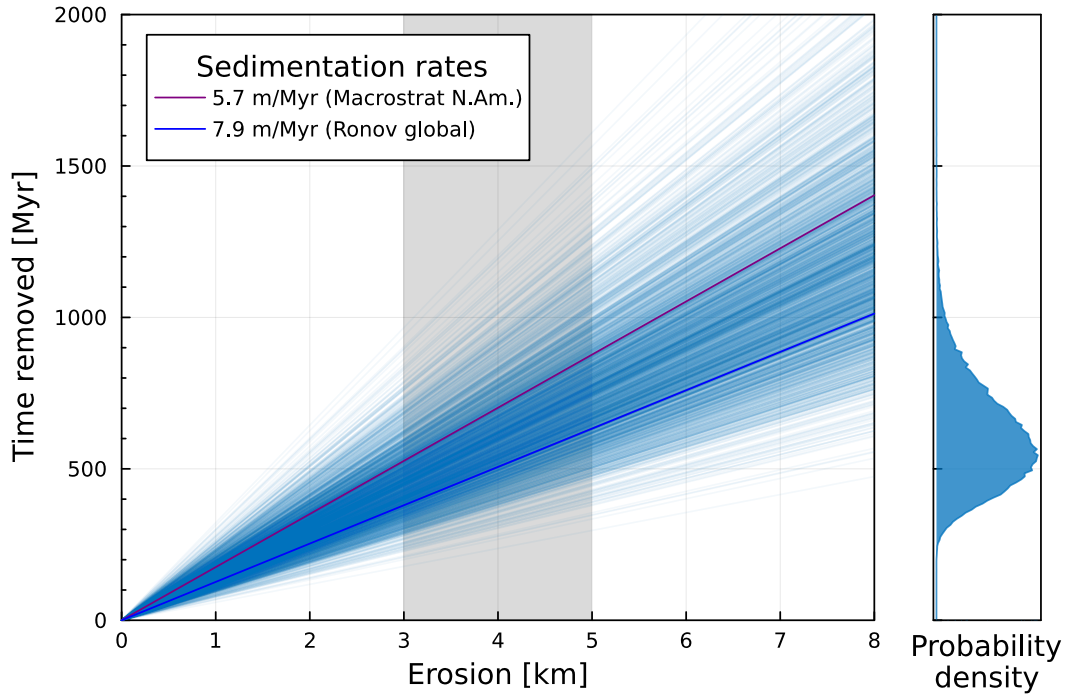



**Figure 9.** Estimates of missing rock from a given time interval due to erosion of the rock record based on vertical sediment accumulation rates. Sedimentation rates derived from the global Phanerozoic mean of  $7.9 \text{ m Myr}^{-1}$  across total continental area (Ronov et al., 1980) and the Macrostrat (Peters et al., 2018) Phanerozoic rate of  $5.7 \text{ m Myr}^{-1}$  across the modern continental area of North America (similar area as Rodinian Laurentia). Monte Carlo simulations (blue lines,  $n = 100,000$ ; 2000 shown) show the amount of ‘missing time’ removed for different total erosion depths using the mean of the Ronov and Macrostrat sedimentation rates ( $6.8 \pm 1.5 \text{ m Myr}^{-1}$ ). Probability density shows the distribution for the amount of time removed. Gray shading highlights the estimated 3–5 km of continental-scale Neoproterozoic erosion predicted from zircon geochemistry (Keller et al., 2019) and thermochronology (McDannell, Keller, et al., 2022b; McDannell & Keller, 2022). Accounting for the full range in sedimentation ( $5.3\text{--}8.4 \text{ m Myr}^{-1}$ ) and 3–5 km of erosion permits removal of a thickness of Precambrian sedimentary rocks extending back to ca. 1060 Ma (min) and 1650 Ma (max). Note the average Ronov global Phanerozoic sediment flux is  $\sim 1.18 \times 10^6 \text{ km}^3 \text{ Myr}^{-1}$  and the North American flux from Macrostrat is  $\sim 1.42 \times 10^5 \text{ km}^3 \text{ Myr}^{-1}$ .

## 8 Conclusions

Inverse thermal history model interpretations reveal sediment deposition and burial patterns across northern Laurentia indicating that exposed crystalline basement and Paleoproterozoic basin remnants underwent comparable burial histories during the Proterozoic that match the composite stratigraphic record preserved along the modern, northern cratonic margin. Our data and models provide independent evidence corroborating the Proterozoic superbasin hypothesis—that areas of basement outside Proterozoic intracratonic basin footprints were also buried beneath a more extensive sedimentary cover during the Columbia and Rodinia supercontinent cycles, including Grenvillian fluvial sandstones that were conceivably deposited across the cratonic interior. Moreover, across all inversions we document substantial erosion of  $\sim 3.3\text{--}5.4$  km between  $< 750$  Ma to  $\geq 600$  Ma, further demonstrating that this period of exhumation contributed to the formation of the Great Unconformity surface. Deep exhumation and dissection of a Proterozoic superbasin by coupled mantle-driven uplift and dynamic ice-sheet activity during the Snowball Earth episodes is also supported by the abrupt appearance of Archean-Paleoproterozoic detrital zircons in Cryogenian strata within Laurentian margin rift basins. Relatively rapid removal and delivery of large volumes of glacially comminuted continental crust ( $> 10^8$  km<sup>3</sup> globally from Keller et al. 2019) to the shelf and deep ocean over a few million years has major implications for secular changes in ocean chemistry (Canfield, 1998), long-term burial of organic carbon (Husson & Peters, 2017), and oxygenation of the atmosphere in the Neoproterozoic (Och & Shields-Zhou, 2012).

## 9 Open Research Section

Data needed to evaluate the conclusions are present in the paper and/or the Supplementary Materials. QTQt models can be retrieved from Open Science Framework:  Plotting and other modeling codes are available from the Github organization *OpenThermochronology*: <https://github.com/OpenThermochronology>.

## Acknowledgments

This work was supported by the Government of Canada Geo-mapping for Energy and Minerals (GEM-2) Program and the NSF Division of Earth Sciences Sedimentary Geo &



Paleobiology program award 2044800 to C.B.K. and K.T.M. The authors thank: W. Davis, N. Rayner, R. Berman, N. Wodicka, & T. Peterson (GSC Ottawa) who facilitated access to archival mineral/rock samples and provided geologic context. J. Metcalf (Univ. of Colorado) & W. Matthews (Univ. of Calgary) for contracted (U-Th)/He analyses. S. Boroughs (WSU) for EPMA. The ideas in this work were initially presented at the September 2023 Thermochronology Conference in Italy. Manuscript in review since April 2024.

CRedit author statement. K.T. McDannell: Conceptualization, Methodology, Formal Analysis, Visualizations, Investigation, Project Management, Data Curation, Software, Writing - Original Draft, Funding Acquisition; C.B. Keller: Software, Writing - Editing, Interpretation; R.H. Rainbird: Validation, Figure 2 drafting, Writing - Editing; K. Dewing: Writing - Editing, Interpretation; J.W. Powell: Sample #4 AFT interpretation, Writing - Editing; P.B. O'Sullivan: Investigation (AFT/U-Pb analyses), Resources.

## References

- Aalto, K. R. (1971). Glacial Marine Sedimentation and Stratigraphy of the Toby Conglomerate (Upper Proterozoic), Southeastern British Columbia, Northwestern Idaho and Northeastern Washington. *Canadian Journal of Earth Sciences*, *8*(7), 753–787. doi: 10.1139/e71-073
- Alexandre, P., Kyser, K., Thomas, D., Polito, P., & Marlat, J. (2009). Geochronology of unconformity-related uranium deposits in the Athabasca Basin, Saskatchewan, Canada and their integration in the evolution of the basin. *Mineralium Deposita*, *44*(1), 41–59. doi: 10.1007/s00126-007-0153-3
- Allen, P. A., & Allen, J. R. (2013). *Basin Analysis: Principles and Application to Petroleum Play Assessment*. John Wiley & Sons.
- Allen, P. A., & Armitage, J. J. (2011). Cratonic Basins. In C. Busby & A. Azor (Eds.), *Tectonics of sedimentary basins* (First ed., pp. 602–620). Wiley. doi: 10.1002/9781444347166.ch30
- Allen, P. A., & Etienne, J. L. (2008). Sedimentary challenge to snowball earth. *Nature Geoscience*, *1*(12), 817–825. doi: 10.1038/ngeo355
- Anderson, A. J., Hodges, K. V., & van Soest, M. C. (2017). Empirical constraints on the effects of radiation damage on helium diffusion in zircon. *Geochimica et Cosmochimica Acta*, *218*, 308–322. doi: 10.1016/j.gca.2017.09.006
- Ault, A. K., Guenther, W. R., Moser, A. C., Miller, G. H., & Refsnider, K. A. (2018).

- Zircon grain selection reveals (de)coupled metamictization, radiation damage, and He diffusivity. *Chemical Geology*, 490, 1–12. doi: 10.1016/j.chemgeo.2018.04.023
- Benn, D. I., Le Hir, G., Bao, H., Donnadieu, Y., Dumas, C., Fleming, E. J., . . . Fairchild, I. J. (2015). Orbitally forced ice sheet fluctuations during the Marinoan Snowball Earth glaciation. *Nature Geoscience*, 8(9), 704–707. doi: 10.1038/ngeo2502
- Bolton, T. E., & Nowlan, G. S. (1979). A Late Ordovician Fossil Assemblage from an Outlier north of Aberdeen Lake, District of Keewatin. *Geological Survey of Canada Bulletin*, 321, 1–26. doi: 10.4095/106171
- Brown, R., Gallagher, K., & Duane, M. (1994). A quantitative assessment of the effects of magmatism on the thermal history of the Karoo sedimentary sequence. *Journal of African Earth Sciences*, 18(3), 227–243. doi: 10.1016/0899-5362(94)90007-8
- Burgess, P. M. (2019). Phanerozoic evolution of the sedimentary cover of the north american craton. In *The sedimentary basins of the united states and canada* (2nd ed., pp. 39–75). Elsevier. doi: 10.1016/B978-0-444-63895-3.00002-4
- Camacho, A., Berman, R., G., & Sanborn-Barrie, M. (2020).  *$^{40}\text{Ar}/^{39}\text{Ar}$  hornblende and biotite cooling ages for metaplutonic rocks of the central Thelon Tectonic Zone, Nunavut* (Tech. Rep.). Geological Survey of Canada. doi: 10.4095/315135
- Canfield, D. E. (1998). A new model for Proterozoic ocean chemistry. *Nature*, 396(6710), 450–453. doi: 10.1038/24839
- Carlson, W. D., Donelick, R. A., & Ketcham, R. A. (1999). Variability of apatite fission-track annealing kinetics: I. Experimental results. *American Mineralogist*, 84(9), 1213–1223. doi: 10.2138/am-1999-0901
- Cawood, P. A., Nemchin, A. A., Smith, M., & Loewy, S. (2003). Source of the Dalradian Supergroup constrained by U–Pb dating of detrital zircon and implications for the East Laurentian margin. *Journal of the Geological Society*, 160(2), 231–246. doi: 10.1144/0016-764902-039
- Cawood, P. A., Nemchin, A. A., Strachan, R., Prave, T., & Krabbendam, M. (2007). Sedimentary basin and detrital zircon record along East Laurentia and Baltica during assembly and breakup of Rodinia. *Journal of the Geological Society*, 164(2), 257–275. doi: 10.1144/0016-76492006-115
- Chi, G., Li, Z., Chu, H., Bethune, K. M., Quirt, D. H., Ledru, P., . . . Potter, E. G. (2018). A shallow-burial mineralization model for the unconformity-related uranium deposits in the Athabasca Basin. *Economic Geology*, 113(5), 1209–1217. doi: 10.5382/

- econgeo.2018.4588
- Chu, H., & Chi, G. (2016). Thermal profiles inferred from fluid inclusion and illite geothermometry from sandstones of the Athabasca basin: Implications for fluid flow and unconformity-related uranium mineralization. *Ore Geology Reviews*, *75*, 284–303. doi: 10.1016/j.oregeorev.2015.12.013
- Cleland, C. E. (2013). Common cause explanation and the search for a smoking gun. In *Rethinking the fabric of geology* (Vol. 502, pp. 1–9). Geological Society of America. doi: 10.1130/2013.2502(01)
- Cogné, N., Chew, D. M., Donelick, R. A., & Ansberque, C. (2020). LA-ICP-MS apatite fission track dating: A practical zeta-based approach. *Chemical Geology*, *531*, 119302. doi: 10.1016/j.chemgeo.2019.119302
- Condon, D. J., Prave, A. R., & Benn, D. I. (2002). Neoproterozoic glacial-rainout intervals: Observations and implications. *Geology*, *30*(1), 35–38. doi: 10.1130/0091-7613(2002)030<0035:NGRIOA>2.0.CO;2
- Cook, S. J., Swift, D. A., Kirkbride, M. P., Knight, P. G., & Waller, R. I. (2020). The empirical basis for modelling glacial erosion rates. *Nature Communications*, *11*(1), 1–7. doi: 10.1038/s41467-020-14583-8
- Cookenboo, H. O., Orchard, M. J., & Daoud, D. K. (1998). Remnants of Paleozoic cover on the Archean Canadian Shield: limestone xenoliths from kimberlite in the central Slave craton. *Geology*, *26*(5), 391–394. doi: 10.1130/0091-7613(1998)026<0391:ROPCOT>2.3.CO;2
- Cox, G. M., Halverson, G. P., Stevenson, R. K., Vokaty, M., Poirier, A., Kunzmann, M., ... Macdonald, F. A. (2016). Continental flood basalt weathering as a trigger for Neoproterozoic Snowball Earth. *Earth and Planetary Science Letters*, *446*, 89–99. doi: 10.1016/j.epsl.2016.04.016
- Creveling, J. R., & Mitrovica, J. X. (2014). The sea-level fingerprint of a Snowball Earth deglaciation. *Earth and Planetary Science Letters*, *399*, 74–85. doi: 10.1016/j.epsl.2014.04.029
- Crowley, K. D. (1991). Thermal history of Michigan Basin and Southern Canadian Shield from apatite fission track analysis. *Journal of Geophysical Research*, *96*(B1), 697–711. doi: 10.1029/90JB02174
- Davis, W. J., Berman, R., Nadeau, L., & Percival, J. (2014). *U-Pb zircon geochronology of a transect across the Thelon Tectonic Zone, Queen Maud region, and adjacent Rae*

- Craton, Kitikmeot region, Nunavut, Canada* (Tech. Rep.). Natural Resources Canada. doi: 10.4095/295177
- Davis, W. J., Gall, Q., Jefferson, C. W., & Rainbird, R. H. (2011). Fluorapatite in the Paleoproterozoic Thelon Basin: Structural-stratigraphic context, in situ ion microprobe U-Pb ages, and fluid-flow history. *Geological Society of America Bulletin*, *123*(5-6), 1056–1073. doi: 10.1130/B30163.1
- DeLucia, M. S., Guenther, W. R., Marshak, S., Thomson, S. N., & Ault, A. K. (2018). Thermochronology links denudation of the Great Unconformity surface to the supercontinent cycle and snowball Earth. *Geology*, *46*(2), 167–170. doi: 10.1130/G39525.1
- Donnadieu, Y., Fluteau, F., Ramstein, G., Ritz, C., & Besse, J. (2003). Is there a conflict between the Neoproterozoic glacial deposits and the snowball Earth interpretation: An improved understanding with numerical modeling. *Earth and Planetary Science Letters*, *208*(1-2), 101–112. doi: 10.1016/S0012-821X(02)01152-4
- Fairchild, I. J., Spencer, A. M., Ali, D. O., Anderson, R. P., Anderton, R., Boomer, I., ... Zhou, Y. (2018). Tonian-Cryogenian boundary sections of Argyll, Scotland. *Precambrian Research*, *319*, 37–64. doi: 10.1016/j.precamres.2017.09.020
- Feinstein, S., Kohn, B., Osadetz, K., Everitt, R., & O’Sullivan, P. (2009). Variable Phanerozoic thermal history in the Southern Canadian Shield: Evidence from an apatite fission track profile at the Underground Research Laboratory (URL), Manitoba. *Tectonophysics*, *475*(1), 190–199. doi: 10.1016/j.tecto.2009.01.016
- Field, M., & Scott Smith, B. H. (1999). Contrasting geology and near-surface emplacement of kimberlite pipes in Southern Africa and Canada. In *The j. b. dawson volume* (Vol. 7; 1, pp. 214–237). Red Roof Design Cape Town.
- Florindo, F., Marra, F., Jicha, B. R., Bulian, F., Di Chiara, A., & Srivastava, P. (2024). Glacier Melting Triggers Massive Gravel Deposition in Central Italy’s River Basins, Unveiling Deglacial Events From 1250 to 780 ka. *Journal of Geophysical Research: Solid Earth*, *129*(3), e2023JB027877. doi: <https://doi.org/10.1029/2023JB027877>
- Flowers, R. M. (2009). Exploiting radiation damage control on apatite (U–Th)/He dates in cratonic regions. *Earth and Planetary Science Letters*, *277*(1-2), 148–155. doi: 10.1016/j.epsl.2008.10.005
- Flowers, R. M., Bowring, S. A., Mahan, K. H., Williams, M. L., & Williams, I. S. (2008). Stabilization and reactivation of cratonic lithosphere from the lower crustal record in the western Canadian shield. *Contributions to Mineralogy and Petrology*, *156*(4),

- 529–549. doi: 10.1007/s00410-008-0301-5
- Flowers, R. M., Ketcham, R. A., Shuster, D. L., & Farley, K. A. (2009). Apatite (U–Th)/He thermochronometry using a radiation damage accumulation and annealing model. *Geochimica et Cosmochimica Acta*, *73*(8), 2347–2365. doi: 10.1016/j.gca.2009.01.015
- Flowers, R. M., MacDonald, F. A., Siddoway, C. S., & Havranek, R. (2020). Diachronous development of Great Unconformities before Neoproterozoic Snowball Earth. *Proceedings of the National Academy of Sciences*, *117*(19), 10172–10180. doi: 10.1073/pnas.1913131117
- Flowers, R. M., Mahan, K. H., Bowring, S. A., Williams, M. L., Pringle, M. S., & Hodges, K. V. (2006). Multistage exhumation and juxtaposition of lower continental crust in the western Canadian Shield: Linking high-resolution U–Pb and  $^{40}\text{Ar}/^{39}\text{Ar}$  thermochronometry with pressure–temperature–deformation paths. *Tectonics*, *25*(4). doi: 10.1029/2005TC001912
- Flowers, R. M., Zeitler, P. K., Danišik, M., Reiners, P. W., Gautheron, C., Ketcham, R. A., ... Brown, R. W. (2023). (U–Th)/He chronology: Part 1. Data, uncertainty, and reporting. *Bulletin of the Geological Society of America*, *135*(1–2), 104–136. doi: 10.1130/B36266.1
- Fraser, J. A., Donaldson, J. A., Fahrig, W. F., & Tremblay, L. P. (1970). Helikian basins and geosynclines of the northwestern Canadian Shield. In A. J. Baer (Ed.), *Symposium on basins and geosynclines of the canadian shield* (Vol. 70, pp. 213–238). Ottawa, Ontario: Geological Survey of Canada, Paper 70-40.
- Furlanetto, F., Thorkelson, D. J., Rainbird, R. H., Davis, W. J., Gibson, H. D., & Marshall, D. D. (2016). The Paleoproterozoic Wernecke Supergroup of Yukon, Canada: Relationships to orogeny in northwestern Laurentia and basins in North America, East Australia, and China. *Gondwana Research*, *39*, 14–40. doi: 10.1016/j.gr.2016.06.007
- Gall, Q. (1992). Precambrian paleosols in Canada. *Canadian Journal of Earth Sciences*, *29*(12), 2530–2536. doi: 10.1139/e92-200
- Gall, Q., & Donaldson, J. A. (2006). Diagenetic fluorapatite and aluminum phosphate–sulphate in the Paleoproterozoic Thelon Formation and Hornby Bay Group, northwestern Canadian Shield. *Canadian Journal of Earth Sciences*, *43*(5), 617–629. doi: 10.1139/e06-011
- Gallagher, K. (2012). Transdimensional inverse thermal history modeling for quantitative thermochronology. *Journal of Geophysical Research: Solid Earth*, *117*(B2). doi: 10

.1029/2011JB008825

- Gallagher, K. (2023). Trans-Dimensional Markov Chain Monte Carlo Methods Applied to Geochronology and Thermochronology. In A. Ismail-Zadeh, D. Jones, F. Castelli, & S. Sanchez (Eds.), *Applications of data assimilation and inverse problems in the earth sciences* (pp. 175–195). Cambridge: Cambridge University Press. doi: 10.1017/9781009180412.012
- Galloway, J. M., Armstrong, D., & Lavoie, D. (2012). Palynology of the INCO Winisk #49204 core (54°18'30"N, 87°02'30"W, NTS 43L/6), Ontario. *Geological Survey of Canada, Open File 7065*, 1–51. doi: 10.4095/290985
- Gautheron, C., Barbarand, J., Ketcham, R. A., Tassan-Got, L., van der Beek, P., Pagel, M., ... Fialin, M. (2013). Chemical influence on  $\alpha$ -recoil damage annealing in apatite: Implications for (U-Th)/He dating. *Chemical Geology*, *351*, 257–267. doi: 10.1016/j.chemgeo.2013.05.027
- Gautheron, C., Djimbi, D. M., Roques, J., Balout, H., Ketcham, R. A., Simoni, E., ... Tassan-Got, L. (2020). A multi-method, multi-scale theoretical study of He and Ne diffusion in zircon. *Geochimica et Cosmochimica Acta*, *268*, 348–367. doi: 10.1016/j.gca.2019.10.007
- Gernon, T. M., Hincks, T. K., Brune, S., Braun, J., Jones, S. M., Keir, D., ... Glerum, A. (2024). Coevolution of craton margins and interiors during continental break-up. *Nature*, *632*(8024), 327–335. doi: 10.1038/s41586-024-07717-1
- Godd ris, Y., Le Hir, G., & Donnadi u, Y. (2011). Chapter 10: Modelling the Snowball Earth. *Geological Society Memoir*, *36*(1), 151–161. doi: 10.1144/M36.10
- Green, P., & Duddy, I. (2021). Discussion: Extracting thermal history from low temperature thermochronology. A comment on recent exchanges between Vermeesch and Tian and Gallagher and Ketcham. *Earth-Science Reviews*, *216*, 103197. doi: 10.1016/j.earscirev.2020.103197
- Green, P., Duddy, I., Gleadow, A., Tingate, P., & Laslett, G. (1985). Fission-track annealing in apatite: Track length measurements and the form of the Arrhenius plot. *Nuclear Tracks and Radiation Measurements (1982)*, *10*(3), 323–328. doi: 10.1016/0735-245X(85)90121-8
- Greenman, J. W., Rooney, A. D., Patzke, M., Ielpi, A., & Halverson, G. P. (2021). Re-Os geochronology highlights widespread latest Mesoproterozoic (ca. 1090–1050 Ma) cratonic basin development on northern Laurentia. *Geology*, *49*(7), 779–783. doi:

- 10.1130/G48521.1
- Guenther, W. R. (2021). Implementation of an Alpha Damage Annealing Model for Zircon (U-Th)/He Thermochronology With Comparison to a Zircon Fission Track Annealing Model. *Geochemistry, Geophysics, Geosystems*, *22*(2). doi: 10.1029/2019GC008757
- Guenther, W. R., Reiners, P. W., Ketcham, R. A., Nasdala, L., & Giester, G. (2013). Helium diffusion in natural zircon: radiation damage, anisotropy, and the interpretation of zircon (U-Th)/He thermochronology. *American Journal of Science*, *313*(3), 145–198. doi: 10.2475/03.2013.01
- Guo, H., Zeitler, P. K., & Idleman, B. D. (2024). Behavior of helium diffusion sinks in apatite: Evidence from continuous ramped heating analysis of borehole and well-characterized samples. *Earth and Planetary Science Letters*, *641*, 118828. doi: 10.1016/j.epsl.2024.118828
- Hadlari, T., Arnott, R. W., Matthews, W. A., Poulton, T. P., Root, K., & Madronich, L. I. (2021). Provenance of the Incipient Passive Margin of NW Laurentia (Neoproterozoic): Detrital Zircon from Continental Slope and Basin Floor Deposits of the Windermere Supergroup, Southern Canadian Cordillera. *Lithosphere*, *2021*, 1–10. doi: 10.2113/2021/8356327
- Hahn, K., Rainbird, R., & Cousens, B. (2013). Sequence stratigraphy, provenance, C and O isotopic composition, and correlation of the late Paleoproterozoic–early Mesoproterozoic upper Hornby Bay and lower Dismal Lakes groups, NWT and Nunavut. *Precambrian Research*, *232*, 209–225. doi: 10.1016/j.precamres.2012.06.001
- Heaman, L. M., LeCheminant, A. N., & Rainbird, R. H. (1992). Nature and timing of Franklin igneous events, Canada: Implications for a Late Proterozoic mantle plume and the break-up of Laurentia. *Earth and Planetary Science Letters*, *109*(1-2), 117–131. doi: 10.1016/0012-821X(92)90078-A
- Hoffman, P. F. (1988). United Plates of America, The Birth of a Craton: Early Proterozoic Assembly and Growth of Laurentia. *Annual Review of Earth and Planetary Sciences*, *16*(1), 543–603. doi: 10.1146/annurev.ea.16.050188.002551
- Hoffman, P. F., Abbot, D. S., Ashkenazy, Y., Benn, D. I., Brocks, J. J., Cohen, P. A., ... Warren, S. G. (2017). Snowball Earth climate dynamics and Cryogenian geology-geobiology. *Science Advances*, *3*(11), e1600983. doi: 10.1126/sciadv.1600983
- Husson, J. M., & Peters, S. E. (2017). Atmospheric oxygenation driven by unsteady growth of the continental sedimentary reservoir. *Earth and Planetary Science Letters*, *460*,

- 68–75. doi: 10.1016/j.epsl.2016.12.012
- Ielpi, A., & Rainbird, R. H. (2015). Architecture and morphodynamics of a 1.6 Ga fluvial sandstone: Ellice Formation of Elu Basin, Arctic Canada. *Sedimentology*, *62*(7), 1950–1977. doi: 10.1111/sed.12211
- Isakson, V. H., Schmitz, M. D., Dehler, C. M., Macdonald, F. A., & Yonkee, W. A. (2022). A robust age model for the Cryogenian Pocatello Formation of southeastern Idaho (northwestern USA) from tandem in situ and isotope dilution U-Pb dating of volcanic tuffs and epiclastic detrital zircons. *Geosphere*, *18*(2), 825–849. doi: 10.1130/GES02437.1
- Issler, D. R., McDannell, K. T., O’Sullivan, P. B., & Lane, L. S. (2022). Simulating sedimentary burial cycles – Part 2: Elemental-based multikinetic apatite fission-track interpretation and modelling techniques illustrated using examples from northern Yukon. *Geochronology*, *4*(1), 373–397. doi: 10.5194/gchron-4-373-2022
- Jefferson, C. W., Thomas, D. J., Gandhi, S. S., Ramaekers, P., Delaney, G., Brisbin, D., ... Olson, R. A. (2007). Unconformity-associated uranium deposits of the Athabasca Basin, Saskatchewan and Alberta. In W. Goodfellow (Ed.), *Mineral deposits of Canada: A synthesis of major deposit-types, district metallogeny, the evolution of geological provinces, and exploration methods* (pp. 273–305). Geological Association of Canada, Mineral Deposits Division.
- Keller, C. B., Husson, J. M., Mitchell, R. N., Bottke, W. F., Gernon, T. M., Boehnke, P., ... Peters, S. E. (2019). Neoproterozoic glacial origin of the Great Unconformity. *Proceedings of the National Academy of Sciences*, *116*(4), 1136–1145. doi: 10.1073/pnas.1804350116
- Kellett, D. A., Pehrsson, S., Skipton, D. R., Regis, D., Camacho, A., Schneider, D. A., & Berman, R. (2020). Thermochronological history of the Northern Canadian Shield. *Precambrian Research*, *342*. doi: 10.1016/j.precamres.2020.105703
- Kepezhinskas, N., Kjarsgaard, B. A., Sarkar, C., Luo, Y., Locock, A. J., & Pearson, D. G. (2024). Petrology, geochemistry, and geochronology of the Mel Kimberlites, Nunavut, Canada and their relationship to Neoproterozoic to Cambrian magmatism in North America. *Mineralogy and Petrology*, 1–20. doi: 10.1007/s00710-024-00876-z
- Ketcham, R. A. (2005). Forward and Inverse Modeling of Low-Temperature Thermochronometry Data. *Reviews in Mineralogy and Geochemistry*, *58*(1), 275–314. doi: 10.2138/rmg.2005.58.11



- Ketcham, R. A., Carter, A., Donelick, R. A., Barbarand, J., & Hurford, A. J. (2007). Improved modeling of fission-track annealing in apatite. *American Mineralogist*, *92*(5-6), 799–810. doi: 10.2138/am.2007.2281
- Ketcham, R. A., Donelick, R. A., & Carlson, W. D. (1999). Variability of apatite fission-track annealing kinetics: III. Extrapolation to geological time scales. *American Mineralogist*, *84*(9), 1235–1255. doi: 10.2138/am-1999-0903
- Kohn, B. P., Gleadow, A. J. W., Brown, R. W., Gallagher, K., Lorencak, M., & Noble, W. P. (2005). Visualizing thermotectonic and denudation histories using apatite fission track thermochronology. In P. W. Reiners & T. A. Ehlers (Eds.), *Reviews in mineralogy and geochemistry* (Vol. 58, pp. 527–565). Mineralogical Society of America and Geochemical Society, Washington, DC, United States (USA). doi: 10.2138/rmg.2005.58.20
- Kolawole, F., & Evenick, J. C. (2023). Global distribution of geothermal gradients in sedimentary basins. *Geoscience Frontiers*, *14*(6), 101685. doi: 10.1016/j.gsf.2023.101685
- Kuhn, M., & Johnson, K. (2013). *Applied Predictive Modeling*. New York, NY: Springer. doi: 10.1007/978-1-4614-6849-3
- Laslett, G. M., Green, P. F., Duddy, I. R., & Gleadow, A. J. (1987). Thermal annealing of fission tracks in apatite 2. A quantitative analysis. *Chemical Geology: Isotope Geoscience Section*, *65*(1), 1–13. doi: 10.1016/0168-9622(87)90057-1
- Lavoie, D., Pinet, N., Zhang, S., Reyes, J., Jiang, C., Ardakani, O., . . . Hahn, K. E. (2019). *Hudson Bay, Hudson Strait, Moose River, and Foxe basins: synthesis of the research activities under the Geomapping for Energy and Minerals (GEM) programs 2008-2018* (Tech. Rep.). Geological Survey of Canada, Open File 8507. doi: 10.4095/314653
- Lawley, C. J., McNicoll, V., Sandeman, H., Pehrsson, S., Simard, M., Castonguay, S., . . . Dubé, B. (2016). Age and geological setting of the Rankin Inlet greenstone belt and its relationship to the gold endowment of the Meliadine gold district, Nunavut, Canada. *Precambrian Research*, *275*, 471–495. doi: 10.1016/j.precamres.2016.01.008
- Le Heron, D. P., Busfield, M. E., & Kamona, F. (2013). An interglacial on snowball Earth? Dynamic ice behaviour revealed in the Chuos Formation, Namibia. *Sedimentology*, *60*(2), 411–427. doi: 10.1111/j.1365-3091.2012.01346.x
- Liu, J., Pearson, D. G., Wang, L. H., Mather, K. A., Kjarsgaard, B. A., Schaeffer, A. J., . . . Armstrong, J. P. (2021). Plume-driven recretionization of deep continental lithospheric

- mantle. *Nature*, *592*(7856), 732–736. doi: 10.1038/s41586-021-03395-5
- Liu, J., Riches, A. J., Pearson, D. G., Luo, Y., Kienlen, B., Kjarsgaard, B. A., . . . Armstrong, J. P. (2016). Age and evolution of the deep continental root beneath the central Rae craton, northern Canada. *Precambrian Research*, *272*, 168–184. doi: 10.1016/j.precamres.2015.11.001
- Liu, Y., & Peltier, W. R. (2013). Sea level variations during snowball Earth formation and evolution: 2. the influence of Earth’s rotation. *Journal of Geophysical Research: Solid Earth*, *118*(8), 4425–4445. doi: 10.1002/jgrb.50294
- Ludwig, K. R. (1998). On the Treatment of Concordant Uranium-Lead Ages. *Geochimica et Cosmochimica Acta*, *62*(4), 665–676. doi: 10.1016/S0016-7037(98)00059-3
- Macdonald, F. A., Schmitz, M. D., Crowley, J. L., Roots, C. F., Jones, D. S., Maloof, A. C., . . . Schrag, D. P. (2010). Calibrating the cryogenian. *Science*, *327*(5970), 1241–1243. doi: 10.1126/science.1183325
- Macdonald, F. A., & Swanson-Hysell, N. L. (2023). The Franklin Large Igneous Province and Snowball Earth Initiation. *Elements*, *19*(5), 296–301. doi: 10.2138/gselements.19.5.296
- Macdonald, F. A., Yonkee, W. A., Flowers, R. M., & Swanson-Hysell, N. L. (2023). Neoproterozoic of Laurentia. In S. J. Whitmeyer, M. L. Williams, D. A. Kellett, & B. Tikoff (Eds.), *Memoir of the geological society of america* (Vol. 220, pp. 331–380). Geological Society of America. doi: 10.1130/2022.1220(19)
- Malinverno, A., & Briggs, V. A. (2004). Expanded uncertainty quantification in inverse problems: Hierarchical Bayes and empirical Bayes. *Geophysics*, *69*(4), 1005–1016. doi: 10.1190/1.1778243
- Masun, K., Doyle, B., Ball, S., & Walker, S. (2004). The geology and mineralogy of the Anuri kimberlite, Nunavut, Canada. *Lithos*, *76*(1-4), 75–97. doi: 10.1016/j.lithos.2004.03.022
- Mazrouei, S., Ghent, R. R., Bottke, W. F., Parker, A. H., & Gernon, T. M. (2019). Earth and Moon impact flux increased at the end of the Paleozoic. *Science*, *363*(6424), 253–257. doi: 10.1126/science.aar4058
- McDannell, K. T., & Flowers, R. M. (2020). Vestiges of the ancient: Deep-time noble gas thermochronology. *Elements*, *16*(5), 325–330. doi: 10.2138/GSELEMENTS.16.5.325
- McDannell, K. T., & Issler, D. R. (2021). Simulating sedimentary burial cycles – Part 1: Investigating the role of apatite fission track annealing kinetics using synthetic data.

- Geochronology*, 3(1), 321–335. doi: 10.5194/gchron-3-321-2021
- McDannell, K. T., & Keller, C. B. (2022). Cryogenian glacial erosion of the central Canadian Shield: The “late” Great Unconformity on thin ice. *Geology*, 50(12), 1336–1340. doi: 10.1130/G50315.1
- McDannell, K. T., Keller, C. B., Guenther, W. R., Zeitler, P. K., & Shuster, D. L. (2022a). Reply to Flowers et al.: Existing thermochronologic data constrain Snowball glacial erosion below the Great Unconformity. *Proceedings of the National Academy of Sciences*, 119(38), e2209946119. doi: 10.1073/pnas.2209946119
- McDannell, K. T., Keller, C. B., Guenther, W. R., Zeitler, P. K., & Shuster, D. L. (2022b). Thermochronologic constraints on the origin of the Great Unconformity. *Proceedings of the National Academy of Sciences*, 119(5), e2118682119. doi: 10.1073/pnas.2118682119
- McDannell, K. T., O’Sullivan, P. B., Gallagher, K., & Boroughs, S. (2022). Phanerozoic sedimentary cover history of the Hudson Platform: a heuristic modeling perspective. *EarthArXiv*, 1–47. doi: 10.31223/X5M05W
- McDannell, K. T., Pinet, N., & Issler, D. R. (2022). Exhuming the Canadian Shield: preliminary interpretations from low-temperature thermochronology and significance for the sedimentary succession of the Hudson Bay Basin. In D. Lavoie & K. Dewing (Eds.), *Sedimentary basins of northern Canada: contributions to a 1000 ma geological journey and insight on resource potential* (pp. 287–322). Natural Resources Canada. doi: 10.4095/326100
- McDannell, K. T., Schneider, D. A., Zeitler, P. K., O’Sullivan, P. B., & Issler, D. R. (2019). Reconstructing deep-time histories from integrated thermochronology: An example from southern Baffin Island, Canada. *Terra Nova*, 31(3), 189–204. doi: 10.1111/ter.12386
- McDannell, K. T., Zeitler, P. K., Janes, D. G., Idleman, B. D., & Fayon, A. K. (2018). Screening apatites for (U-Th)/He thermochronometry via continuous ramped heating: He age components and implications for age dispersion. *Geochimica et Cosmochimica Acta*, 223, 90–106. doi: 10.1016/j.gca.2017.11.031
- McDannell, K. T., Zeitler, P. K., & Schneider, D. A. (2018). Instability of the southern Canadian Shield during the late Proterozoic. *Earth and Planetary Science Letters*, 490, 100–109. doi: 10.1016/j.epsl.2018.03.012
- McKay, R., Enkelmann, E., Hadlari, T., Matthews, W., & Mouthereau, F. (2021). Ceno-

- zoic Exhumation History of the Eastern Margin of the Northern Canadian Cordillera. *Tectonics*, *40*(4), e2020TC006582. doi: 10.1029/2020TC006582
- McMechan, M. E. (2000). Vreeland diamictites - Neoproterozoic glaciogenic slope deposits, Rocky Mountains, northeast British Columbia. *Bulletin of Canadian Petroleum Geology*, *48*(3), 246–261. doi: 10.2113/48.3.246
- Mills, B., Watson, A. J., Goldblatt, C., Boyle, R., & Lenton, T. M. (2011). Timing of Neoproterozoic glaciations linked to transport-limited global weathering. *Nature Geoscience*, *4*(12), 861–864. doi: 10.1038/ngeo1305
- Mitchell, R. N., Gernon, T. M., Cox, G. M., Nordsvan, A. R., Kirscher, U., Xuan, C., ... He, X. (2021). Orbital forcing of ice sheets during snowball Earth. *Nature Communications*, *12*(1), 4187. doi: 10.1038/s41467-021-24439-4
- Moles, N., & Selby, D. (2023). Implications of new geochronological constraints on the Aberfeldy stratiform barite deposits, Scotland, for the depositional continuity and global correlation of the Neoproterozoic Dalradian Supergroup. *Precambrian Research*, *384*, 106925. doi: 10.1016/j.precamres.2022.106925
- Och, L. M., & Shields-Zhou, G. A. (2012). The Neoproterozoic oxygenation event: Environmental perturbations and biogeochemical cycling. *Earth-Science Reviews*, *110*(1-4), 26–57. doi: 10.1016/j.earscirev.2011.09.004
- Ojha, L., Troncone, B., Buffo, J., Journaux, B., & McDonald, G. (2022). Liquid water on cold exo-Earths via basal melting of ice sheets. *Nature Communications*, *13*(1), 7521. doi: 10.1038/s41467-022-35187-4
- Osadetz, K., Kohn, B., Feinstein, S., & O'Sullivan, P. (2002). Thermal history of Canadian Williston basin from apatite fission-track thermochronology—implications for petroleum systems and geodynamic history. *Tectonophysics*, *349*(1-4), 221–249. doi: 10.1016/S0040-1951(02)00055-0
- Patton, H., Hubbard, A., Heyman, J., Alexandropoulou, N., Lasabuda, A. P., Stroeven, A. P., ... Andreassen, K. (2022). The extreme yet transient nature of glacial erosion. *Nature Communications*, *13*(1), 7377. doi: 10.1038/s41467-022-35072-0
- Peak, B. A., Flowers, R. M., & Macdonald, F. A. (2023). Ediacaran-Ordovician tectonic and geodynamic drivers of Great Unconformity exhumation on the southern Canadian Shield. *Earth and Planetary Science Letters*, *619*, 118334. doi: 10.1016/j.epsl.2023.118334
- Pehrsson, S. J., Berman, R. G., Eglington, B., & Rainbird, R. (2013). Two Neoproterozoic

- supercontinents revisited: The case for a Rae family of cratons. *Precambrian Research*, 232, 27–43. doi: 10.1016/j.precamres.2013.02.005
- Pehrsson, S. J., Eglington, B., Rainbird, R., Regis, D., Ramaekers, P., & Jefferson, C. (2023). Extent and significance of the Racklan–Forward Orogen in Canada: far-field interior reactivation during Nuna assembly. *Geological Society, London, Special Publications*, 531(1), SP531–2022–307. doi: 10.1144/sp531-2022-307
- Peters, S. E., Husson, J. M., & Czaplewski, J. (2018). Macrostrat: A Platform for Geological Data Integration and Deep-Time Earth Crust Research. *Geochemistry, Geophysics, Geosystems*, 19(4), 1393–1409. doi: 10.1029/2018GC007467
- Powell, J., Schneider, D., Stockli, D., & Fallas, K. (2016). Zircon (U-Th)/He thermochronology of Neoproterozoic strata from the Mackenzie Mountains, Canada: Implications for the Phanerozoic exhumation and deformation history of the northern Canadian Cordillera. *Tectonics*, 35(3), 663–689. doi: 10.1002/2015TC003989
- Prave, A. R., Fallick, A. E., Thomas, C. W., & Graham, C. M. (2009). A composite C-isotope profile for the Neoproterozoic Dalradian Supergroup of Scotland and Ireland. *Journal of the Geological Society*, 166(5), 845–857. doi: 10.1144/0016-76492008-131
- Pu, J. P., Macdonald, F. A., Schmitz, M. D., Rainbird, R. H., Bleeker, W., Peak, B. A., ... Hamilton, M. A. (2022). Emplacement of the Franklin large igneous province and initiation of the Sturtian Snowball Earth. *Science Advances*, 8(47), eadc9430. doi: 10.1126/sciadv.adc9430
- Rainbird, R. H. (1993). The Sedimentary Record of Mantle Plume Uplift Preceding Eruption of the Neoproterozoic Natkusiak Flood Basalt. *The Journal of Geology*, 101(3), 305–318. doi: 10.1086/648225
- Rainbird, R. H., Cawood, P., & Gehrels, G. (2012). The Great Grenvillian Sedimentation Episode: Record of Supercontinent Rodinia’s assembly. In *Tectonics of sedimentary basins: Recent advances* (pp. 583–601). Wiley. doi: 10.1002/9781444347166.ch29
- Rainbird, R. H., & Davis, W. J. (2007). U-Pb detrital zircon geochronology and provenance of the late Paleoproterozoic Dubawnt Supergroup: Linking sedimentation with tectonic reworking of the western Churchill Province, Canada. *Geological Society of America Bulletin*, 119(3-4), 314–328. doi: 10.1130/b25989.1
- Rainbird, R. H., & Davis, W. J. (2022). On the Statherian–Calymmian palaeogeography of northwestern Laurentia. *Journal of the Geological Society*, 179(5), jgs2022–062. doi: 10.1144/jgs2022-062

- Rainbird, R. H., & Ernst, R. E. (2001). The sedimentary record of mantle-plume uplift. In *Special paper of the geological society of america* (Vol. 352, pp. 227–245). Geological Society of America. doi: 10.1130/0-8137-2352-3.227
- Rainbird, R. H., Hadlari, T., Aspler, L., Donaldson, J., LeCheminant, A., & Peterson, T. (2003). Sequence stratigraphy and evolution of the Paleoproterozoic intracontinental Baker Lake and Thelon basins, western Churchill Province, Nunavut, Canada. *Precambrian Research*, 125(1-2), 21–53. doi: 10.1016/S0301-9268(03)00076-7
- Rainbird, R. H., Heaman, L. M., & Young, G. (1992). Sampling Laurentia: detrital zircon geochronology offers evidence for an extensive Neoproterozoic river system originating from the Grenville orogen. *Geology*, 20(4), 351–354. doi: 10.1130/0091-7613(1992)020<0351:SLDZGO>2.3.CO;2
- Rainbird, R. H., Jefferson, C. W., & Young, G. M. (1996). The early Neoproterozoic sedimentary Succession B of northwestern Laurentia: Correlations and paleogeographic significance. *Geological Society of America Bulletin*, 108(4), 454–470. doi: 10.1130/0016-7606(1996)108<0454:TENSSB>2.3.CO;2
- Rainbird, R. H., Rayner, N., Hadlari, T., Heaman, L., Ielpi, A., Turner, E., & MacNaughton, R. (2017). Zircon provenance data record the lateral extent of pancontinental, early Neoproterozoic rivers and erosional unroofing history of the Grenville orogen. *GSA Bulletin*, 129(11-12), 1408–1423. doi: 10.1130/B31695.1
- Rainbird, R. H., Rooney, A. D., Creaser, R. A., & Skulski, T. (2020). Shale and pyrite Re-Os ages from the Hornby Bay and Amundsen basins provide new chronological markers for Mesoproterozoic stratigraphic successions of northern Canada. *Earth and Planetary Science Letters*, 548, 116492. doi: 10.1016/j.epsl.2020.116492
- Rainbird, R. H., Stern, R. A., Rayner, N., & Jefferson, C. W. (2007). Age, provenance, and regional correlation of the Athabasca Group, Saskatchewan and Alberta, constrained by igneous and detrital zircon geochronology. *Bulletin of the Geological Survey of Canada*, 588(588), 193–209. doi: 10.4095/223761
- Ramaekers, P., Jefferson, C. W., Yeo, G. M., Collier, B., Long, D. G. F., Drever, G., ... Wheatley, K. (2007). Revised geological map and stratigraphy of the Athabasca Group, Saskatchewan and Alberta. In C. Jefferson & G. Delaney (Eds.), *Extech iv: Geology and uranium exploration technology of the proterozoic athabasca basin, saskatchewan and alberta, geological survey of canada bulletin* (Vol. 588, pp. 155–191). Natural Resources Canada. doi: 10.4095/223754

- Regis, D., Pehrsson, S., Martel, E., Thiessen, E., Peterson, T., & Kellett, D. (2021). Post-1.9 Ga evolution of the south Rae craton (Northwest Territories, Canada): A Paleoproterozoic orogenic collapse system. *Precambrian Research*, *355*, 106105. doi: 10.1016/j.precamres.2021.106105
- Reiners, P. W., Carlson, R. W., Renne, P. R., Cooper, K. M., Granger, D. E., McLean, N. M., & Schoene, B. (2017). The (U–Th)/He system. In *Geochronology and thermochronology* (pp. 291–363). John Wiley & Sons. doi: <https://doi.org/10.1002/9781118455876.ch11>
- Rieu, R., Allen, P. A., Plötze, M., & Pettke, T. (2007). Climatic cycles during a Neoproterozoic "snowball" glacial epoch. *Geology*, *35*(4), 299–302. doi: 10.1130/G23400A.1
- Ronov, A. B., Khain, V. E., Balukhovskiy, A. N., & Seslavinsky, K. B. (1980). Quantitative analysis of Phanerozoic sedimentation. *Sedimentary Geology*, *25*(4), 311–325. doi: 10.1016/0037-0738(80)90067-6
- Rooney, A. D., Chew, D. M., & Selby, D. (2011). Re–Os geochronology of the Neoproterozoic–Cambrian Dalradian Supergroup of Scotland and Ireland: Implications for Neoproterozoic stratigraphy, glaciations and Re–Os systematics. *Precambrian Research*, *185*(3-4), 202–214. doi: 10.1016/j.precamres.2011.01.009
- Rooney, A. D., Strauss, J. V., Brandon, A. D., & Macdonald, F. A. (2015). A Cryogenian chronology: Two long-lasting synchronous Neoproterozoic glaciations. *Geology*, *43*(5), 459–462. doi: 10.1130/G36511.1
- Ross, G. M. (1991). Tectonic setting of the Windermere Supergroup revisited. *Geology*, *19*(11), 1125–1128. doi: 10.1130/0091-7613(1991)019<1125:TSOTWS>2.3.CO;2
- Ross, G. M., Villeneuve, M. E., & Theriault, R. J. (2001). Isotopic provenance of the lower Muskwa assemblage (Mesoproterozoic, Rocky Mountains, British Columbia): New clues to correlation and source areas. *Precambrian Research*, *111*(1-4), 57–77. doi: 10.1016/S0301-9268(01)00156-5
- Sanford, B. (1987). Paleozoic Geology of the Hudson Platform. In C. Beaumont & A. Tankard (Eds.), *Sedimentary basins and basin-forming mechanisms* (Vol. Memoir 12, pp. 483–505). Canadian Society of Petroleum Geologists.
- Schumer, R., & Jerolmack, D. J. (2009). Real and apparent changes in sediment deposition rates through time. *Journal of Geophysical Research*, *114*(3), F00A06. doi: 10.1029/2009JF001266
- Schwab, F. L. (1976). Modern and ancient sedimentary basins: Comparative accumulation

- rates. *Geology*, 4(12), 723–727. doi: 10.1130/0091-7613(1976)4<723:MAASBC>2.0.CO;2
- Shipman, S., Rainbird, R., & Rooney, A. D. (2024). Re-Os Geochronology and Os-Sr Isotope Data for the Bitter Springs Excursion, Wynniatt Formation, Shaler Supergroup, Canada. In *Geological society of america abstracts with programs* (p. 1). Boulder, CO, United States: Geological Society of America.
- Sloss, L. L. (1963). Sequences in the cratonic interior of North America. *Geological Society of America Bulletin*, 74(2), 93–114. doi: 10.1130/0016-7606(1963)74[93:SITCIO]2.0.CO;2
- Sloss, L. L. (1988). Tectonic evolution of the craton in Phanerozoic time. In L. L. Sloss (Ed.), *Sedimentary cover—north american craton* (Vol. D-2, pp. 25–51). Boulder, Colorado: Geological Society of America. doi: 10.1130/DNAG-GNA-D2.25
- Smith, M. D., Arnaud, E., Arnott, R. W., & Ross, G. M. (2011). The record of Neoproterozoic glaciations in the Windermere Supergroup, southern Canadian Cordillera. *Geological Society Memoir*, 36(1), 413–424. doi: 10.1144/M36.37
- Steinberger, B., & Becker, T. W. (2018). A comparison of lithospheric thickness models. *Tectonophysics*, 746, 325–338. doi: 10.1016/j.tecto.2016.08.001
- Stephenson, J., Gallagher, K., & Holmes, C. (2006). A Bayesian approach to calibrating apatite fission track annealing models for laboratory and geological timescales. *Geochimica et Cosmochimica Acta*, 70(20), 5183–5200. doi: 10.1016/j.gca.2006.07.027
- Stephenson, S. N., Ball, P. W., & Richards, F. D. (2023). Destruction and regrowth of lithospheric mantle beneath large igneous provinces. *Science Advances*, 9(36), eadf6216. doi: 10.1126/sciadv.adf6216
- Strachan, R. A., Prave, A. R., Kirkland, C. L., & Storey, C. D. (2013). U-Pb detrital zircon geochronology of the Dalradian Supergroup, Shetland Islands, Scotland: Implications for regional correlations and Neoproterozoic-Palaeozoic basin development. *Journal of the Geological Society*, 170(6), 905–916. doi: 10.1144/jgs2013-057
- Tappe, S., Kjarsgaard, B. A., Kurszlaukis, S., Nowell, G. M., & Phillips, D. (2014). Petrology and Nd-Hf isotope geochemistry of the Neoproterozoic Amon kimberlite sills, Baffin Island (Canada): Evidence for deep mantle magmatic activity linked to supercontinent cycles. *Journal of Petrology*, 55(10), 2003–2042. doi: 10.1093/petrology/egu048
- Thurston, O., Guenther, W., Karlstrom, K., Heizler, M., Ricketts, J., & McDannell, K. (2024). Deep-time thermal history of the Great Unconformity in the Grand Canyon,



- USA: Combined zircon (U-Th)/He and K-feldspar  $^{40}\text{Ar}/^{39}\text{Ar}$  thermochronometers. *Geological Society of America Bulletin*, *136*(11-12), 4815–4835. doi: 10.1130/B37358.1
- Thybo, H., & Artemieva, I. (2013). Moho and magmatic underplating in continental lithosphere. *Tectonophysics*, *609*, 605–619. doi: 10.1016/j.tecto.2013.05.032
- Vermeesch, P. (2018). IsoplotR: A free and open toolbox for geochronology. *Geoscience Frontiers*, *9*(5), 1479–1493. doi: 10.1016/j.gsf.2018.04.001
- Vermeesch, P., & Tian, Y. (2014). Thermal history modelling: HeFTy vs. QTQt. *Earth-Science Reviews*, *139*, 279–290. doi: 10.1016/j.earscirev.2014.09.010
- Walter, M. R., Veevers, J. J., Calver, C. R., & Grey, K. (1995). Neoproterozoic stratigraphy of the Centralian Superbasin, Australia. *Precambrian Research*, *73*(1-4), 173–195. doi: 10.1016/0301-9268(94)00077-5
- Wang, C., Mitchell, R. N., Murphy, J. B., Peng, P., & Spencer, C. J. (2021). The role of megacontinents in the supercontinent cycle. *Geology*, *49*(4), 402–406. doi: 10.1130/G47988.1
- Wang, Y., Cao, Z., Peng, L., Liu, L., Chen, L., Lundstrom, C., . . . Yang, X. (2023). Secular craton evolution due to cyclic deformation of underlying dense mantle lithosphere. *Nature Geoscience*, *16*(7), 637–645. doi: 10.1038/s41561-023-01203-5
- Webb, K., Harder, M., Holmes, P., Baumgartner, M. C., & Pell, J. (2008). The geology of the Nanuq kimberlites: new textural varieties in the Western Churchill Province, Canada. In *International kimberlite conference extended abstracts: 2008* (Vol. 9, pp. 1–3). Frankfurt, Germany: University of Alberta. doi: 10.29173/ikc3534
- Wilner, J. A., Nordin, B. J., Getraer, A., Gregoire, R. M., Krishna, M., Li, J., . . . Keller, C. (2024). Limits to timescale dependence in erosion rates: Quantifying glacial and fluvial erosion across timescales. *Science Advances*, *10*(51), eadr2009. doi: 10.1126/sciadv.adr2009
- Young, G. M. (1979). Correlation of middle and upper Proterozoic strata of the northern rim of the North Atlantic craton. *Earth and Environmental Science Transactions of the Royal Society of Edinburgh*, *70*(13-14), 323–336. doi: 10.1017/S0080456800012849
- Zhang, S. (2011). Timing and extent of maximum transgression across Laurentia during Late Ordovician: New evidence from Slave Craton, Canadian Shield. *Palaeogeography, Palaeoclimatology, Palaeoecology*, *306*(3-4), 196–204. doi: 10.1016/j.palaeo.2011.04.019